

1 **Tumor-educated Gr1⁺CD11b⁺ cells instigate breast cancer metastasis by twisting**
2 **cancer cells plasticity via OSM/IL6–JAK signaling**

3
4 Sanam Peyvandi^{1, +, *}, Manon Bulliard^{1, +}, Annamaria Kauzlaric², Oriana Coquoz¹, Yu-Ting
5 Huang¹, Nathalie Duffey^{1, +}, Laetitia Gafner¹, Gireca Lorusso¹, Nadine Fournier², Qiang
6 Lan^{1,3,*,#}, and Curzio Rüegg^{1,*,#}

7
8 ¹ Pathology Unit, Department of Oncology, Microbiology and Immunology (OMI), Faculty
9 of Science and Medicine, University of Fribourg, 1700 Fribourg, Switzerland;

10 ² Translational Data Science Group, Swiss Institute of Bioinformatics, Lausanne,
11 Switzerland;

12 ³ Cell and Tissue Dynamics Research Program, Institute of Biotechnology, Helsinki
13 Institute of Life Science (HiLIFE), University of Helsinki, Helsinki, Finland.

14

15 * These authors contributed equally as corresponding authors.

16

17

18 + Current affiliations: S.P., Immunobiology Department, University of Lausanne (UNIL),
19 Switzerland; M.B., Swiss Institute for Experimental Cancer Research (ISREC), Ecole
20 Polytechnique Fédérale Lausanne (EPFL) UPCDA SV 2833 (Bâtiment SV) Lausanne,
21 Switzerland; N.D., Department of Oncology, Centre Hospitalier Universitaire Vaudois
22 (CHUV), University of Lausanne (UNIL), Switzerland; Y-T.H., Daiichi Sankyo Co., Ltd.
23 Taipei City, Taiwan

24

25 # Lead contacts and co-senior authors:

26 # C.R. (curzio.ruegg@unifr.ch; +4126 300 8766), Department of Oncology, Microbiology,
27 Immunology, Faculty of Science and Medicine, University of Fribourg, Chemin du Musée
28 18, Per 17, CH-1700 Fribourg, Switzerland

29 # Q.L. (qiang.lan@helsinki.fi) Cell and Tissue Dynamics Research Program, Institute of
30 Biotechnology, Helsinki Institute of Life Science (HiLIFE), Biocenter 2, P.O. Box 56,
31 FIN-00014, University of Helsinki, Helsinki, Finland

32

33 **Running title:** OMS/IL6 twist breast cancer plasticity to promote metastasis

34

35 **Keywords:** Breast cancer metastasis, chemotherapy, cancer stem cells, GR1, Oncostatin
36 M, IL6, JAK, plasticity, heterogeneity

37

38 **Abstract**

39 Cancer cell plasticity contributes to tumor therapy resistance and metastasis formation,
40 which represent the main causes of cancer-related death for most cancers, including
41 breast cancer. The tumor microenvironment drives cancer cell plasticity and metastasis
42 and unravelling the underlying cues may provide novel effective strategies to manage
43 metastatic disease. Here we show that stem cell antigen-1 positive (Sca-1⁺) murine breast
44 cancer cells enriched during tumor progression and metastasis have higher *in vitro* cancer
45 stem cell-like properties, enhanced *in vivo* metastatic ability, and initiate primary tumors
46 rich in Gr1^{high}CD11b⁺Ly6C^{low} cells. In turn, tumor-educated Gr1⁺CD11b⁺ (Tu-Gr1⁺CD11b⁺)
47 cells rapidly and transiently convert low metastatic 4T1-Sca-1⁻ cells into highly metastatic
48 4T1-Sca-1⁺ cells via secreted OSM and IL6. Moreover, chemotherapy-resistant and highly
49 metastatic 4T1-derived cells maintain high Sca-1⁺ frequency through cell autonomous IL6
50 production. Inhibition of OSM, IL6 or JAK suppressed Tu-Gr1⁺CD11b⁺-induced Sca-1⁺
51 population enrichment *in vitro*, while JAK inhibition abrogated metastasis of chemotherapy-
52 enriched Sca-1⁺ cells *in vivo*. Importantly, Tu-Gr1⁺CD11b⁺ cells invoked a gene signature
53 in tumor cells predicting shorter OS and RFS in breast cancer patients. Collectively, our
54 data identified OSM/IL6-JAK as a clinically relevant paracrine/autocrine axis instigating
55 breast cancer cell plasticity triggering metastasis.

56

57 Introduction

58 Metastasis accounts for over 90% of cancer-related death, calling for new strategies
59 to prevent cancer cell dissemination and metastasis formation ¹. Recent studies using
60 single-cell lineage tracing and single-cell RNA sequencing (scRNA-seq) technologies have
61 provided detailed information about intratumor heterogeneity ^{2,3}, whereby genetically,
62 epigenetically and functionally diverse subpopulations of cancer cells exist within the tumor
63 mass, spatially and temporally ⁴. Intratumor heterogeneity may arise by modulating cancer
64 cell plasticity, especially of cancer stem cells (CSCs), through cell-intrinsic and -extrinsic
65 mechanisms ^{5,6}.

66 Multiple CSC subpopulations appear to co-exist within the primary tumor mass
67 resulting in high degree of tumor cell heterogeneity and increased aggressiveness ⁷
68 including in breast cancer ^{4,8–11}. In particular, CSCs can acquire metastasis initiating
69 capacities ¹² and resistance to therapy, resulting in cancer relapse ⁴. Moreover, non-CSCs
70 within the tumor bulk may acquire CSC properties to repopulate the tumor⁴. While CSC are
71 defined rather functionally by their ability to initiate tumors and metastasis in low number
72 *in vivo*, several cell surface markers associated with CSC features have been reported,
73 including CD44, CD24, Sca-1, CD61, CD49f were used to identify breast CSCs ^{13,14}.

74 The interaction of tumor cells with the tumor microenvironment (TME) contributes to
75 tumor cell plasticity and tumor heterogeneity ^{15,16}. Cells of the TME also promote tumor
76 escape and metastasis through multiple mechanisms, including promotion of
77 angiogenesis, cell survival, invasion, epithelial-mesenchymal transition (EMT), and
78 immunosuppression ^{17–22}. Recently, they have been reported to instigate expansion of
79 CSC with metastatic ability (also known as metastasis-initiating cells) in different cancers
80 ^{17,23,24}. Thus, the TME dynamics is a key driver of cancer cell plasticity and heterogeneity
81 promoting tumor growth, progression and metastasis ⁴. Accurate characterization of the

82 regulation of tumor plasticity and heterogeneity by the TME may reveal novel opportunities
83 for developing effective anti-metastatic therapies ^{8,14}.

84 TME-derived Oncostatin M (OSM) has been shown to mediate tumor progression
85 and CSC stemness by activating its receptor OSMR ²⁵. OSM belongs to the IL6 family of
86 cytokines (including IL6 itself, IL11 and LIF) ^{26,27}, whose members bind to dimeric receptors
87 sharing a common subunit (gp130 or IL6ST) and activate JAK-STAT, RAS-MAPK and
88 PI3K-AKT pathways ^{28,29}. Increased OSM or IL6 expression correlates with reduced
89 survival in breast cancer patients ^{30,31}. OSM was shown to drive breast cancer progression
90 and metastasis through direct effects on cancer cells, such as suppression of estrogen
91 receptor (ER) expression ³¹ and promotion of EMT ^{25,32}, and indirect effects via TME cells,
92 in particular the reprogramming of tumor associated macrophages and fibroblasts ^{33–36}.

93 Here, by assessing the metastatic evolution of murine triple-negative breast cancer
94 (TNBC) models *in silico* and *in vivo*, we observed that the Sca-1⁺ tumor cell subpopulation
95 is enriched during tumor progression. We show that tumor-educated Gr1⁺CD11b⁺ cells
96 (Tu-Gr1⁺CD11b⁺), but not naïve Gr1⁺CD11b⁺ cells from spleen (Spl-Gr1⁺CD11b⁺) or bone
97 marrow (BM-Gr1⁺CD11b⁺) in tumor-bearing mice, modulate tumor plasticity via OSM/IL6-
98 JAK signaling by rapidly and transiently converting 4T1-Sca-1⁻ cells into 4T1-Sca-1⁺ cells
99 with high metastatic capacity. Prolonged exposure of 4T1 cells to chemotherapy stably
100 enriched for metastatic Sca-1⁺ cells via an autocrine IL6-JAK signaling loop. A short *in vitro*
101 treatment of these chemo-resistant cells with the JAK inhibitor Ruxolitinib, suppressed their
102 metastatic capacity. Importantly, Tu-Gr1⁺CD11b⁺ invoked a gene expression signature in
103 4T1 cells that predicted shorter overall survival (OS) and relapse-free survival (RFS) in
104 breast cancer patients, reinforcing the clinical relevance of these findings.

105 Our results reveal a novel mechanism modulating tumor plasticity and triggering the
106 emergence of cancer cells with enhanced metastatic capacity, through paracrine (Tu-

107 Gr1⁺CD11b⁺-mediated) and cell autonomous (chemotherapy-induced) OSM/IL6-JAK
108 dependent signaling. The OSM/IL6-JAK axis may be considered as a candidate of
109 actionable clinical targets to impinge on metastatic progression and therapy resistance.

110

111 **Results**

112 **The Sca-1⁺ population is enriched during tumor progression and has higher *in vivo*** 113 **metastatic capacity**

114 To investigate tumor cell heterogeneity during tumor progression, we first examined
115 the expression of the previously reported breast CSC markers CD24, CD44, CD61, Sca-1
116 and CD49f¹³ in the publicly available RNA sequencing (RNAseq) dataset from Ross *et al.*
117 encompassing several murine breast cancer models³⁷. This dataset includes data from
118 cultured cancer cells (In_Culture), orthotopic primary tumors (OT_PT), spontaneous lung
119 metastases (OT_LuM), and experimental lung metastases after tail vein injection
120 (TV_LuM) (Fig. 1a and Supplementary Fig. 1a). *Sca-1* expression was elevated in lung
121 metastasis in 4T1, 6DT1, Mvt1 and Met1 models compared with the respective primary
122 tumors. Interestingly, in 4T1, 6DT1 and Mvt1 models, *Sca-1* expression was also elevated
123 in experimental lung metastases compared with cultured cells. However, the expression of
124 *Cd24*, *Cd44*, *Cd61* and *Cd49f* were not altered, or their expression pattern was inconsistent
125 during progression (Supplementary Fig. 1a). Thus, increased *Sca-1* expression during
126 metastasis is consistently observed in different preclinical breast cancer models.

127 To investigate whether the increased *Sca-1* expression within the tumor mass was
128 due to an increased gene expression in all cancer cells or to the enrichment of a Sca-1⁺
129 population, we orthotopically injected 4T1 tumor cells and determined the frequency of
130 different cell populations present in the primary tumor and lung metastases 30 days later
131 by flow cytometry (Fig. 1b). We observed that the frequency of both Sca-1⁺ and CD61⁺

132 populations increased in lung metastases compared to primary tumors (Fig. 1c). In
133 contrast, the CD24⁺, CD44⁺ and CD49f⁺ populations were not significantly altered.

134 The enrichment of the Sca-1⁺ population in lung metastases prompted us to ask
135 whether Sca-1⁺ cells actively contribute to the metastasis. To this end, we isolated 4T1-
136 Sca-1⁺ and 4T1-Sca-1⁻ cells by magnetic activated cell sorting (MACS) from parental 4T1
137 cells, which contains low frequency of Sca-1⁺ population (10-15%) (Supplementary Fig.
138 1b, c), and examined their metastatic ability *in vivo*. In the orthotopic injection model, 4T1-
139 Sca-1⁺ cells formed significantly more lung metastases than 4T1-Sca-1⁻ cells, while there
140 was no significant difference in primary tumor growth (Fig. 1d-f). Upon tail vein injection,
141 4T1-Sca-1⁺ cells displayed significantly greater lung colonization ability compared to 4T1-
142 Sca-1⁻ cells and a non-significant increase compared to parental 4T1 cells (Fig. 1g-i). In
143 addition, 4T1-Sca-1⁺ cells showed significantly higher *in vitro* mammosphere forming
144 efficiency than 4T1-Sca-1⁻ cells (Supplementary Fig. 2a), while *in vitro* cell growth,
145 anchorage-independent survival, and cell motility were comparable (Supplementary Fig.
146 2b-d).

147 These results suggest that 4T1-Sca-1⁺ and 4T1-Sca-1⁻ cells have similar tumorigenic
148 potential, while 4T1-Sca-1⁺ cells have higher metastasis-initiating capacity.

149

150 **The Sca-1⁺ population is plastic *in vitro* and *in vivo***

151 Growing evidence indicates that cancer cells possess plastic features, which can be
152 modulated by both cell-intrinsic factors and microenvironmental cues^{37,38}. To characterize
153 the observed plasticity of 4T1-Sca-1⁺ cells, we first investigated isolated 4T1-Sca-1⁺ and
154 4T1-Sca-1⁻ cells *in vitro*. The abundance of Sca-1⁺ population in 4T1-Sca-1⁺ cells enriched
155 by MACS sorting (> 75%) gradually decreased to 50% after 4 days of culture
156 (Supplementary Fig. 2e, upper panel), while the Sca-1⁻ cells (negatively enriched by

157 MACS) regenerated a Sca-1⁺ population (from less than 1% to 19%) (Supplementary Fig.
158 2e, lower panel). Consistently, after orthotopic injection of 4T1-Sca-1⁺ cells, the abundance
159 of the Sca-1⁺ population in the derived tumors decreased from 75% to about 40% after 23
160 days of growth, while in tumors generated from 4T1-Sca-1⁻ cells it increased from less than
161 1% to 15% (Supplementary Fig. 2f), similar to the frequency of Sca-1⁺ population in tumors
162 derived from parental 4T1 cells (Fig. 1c). In addition, when tumor cells derived from primary
163 tumors and lung metastases of parental 4T1-injected mice were cultured *ex vivo*, the
164 abundance of the Sca-1⁺ population significantly decreased from 20% to 4.5% and 60% to
165 19%, respectively (Supplementary Fig. 2g).

166 From these observations we conclude that both Sca-1⁺ and Sca-1⁻ populations are
167 highly plastic and this plasticity appears to be modulated *in vivo*.

168

169 **Tumor-educated Gr1⁺CD11b⁺ cells expand the metastatic Sca-1⁺ population**

170 Immune cells in the TME are critical determinants of tumor cells functions and
171 behaviors, including metastatic capacity³⁹. To collect evidence for a potential correlation
172 between immune cells and the Sca-1⁺ population, we characterized the inflammatory cells
173 infiltrating the orthotopic primary tumors. We observed a significant increase of the
174 Gr1^{high}CD11b⁺Ly6C^{low} population and a significant decrease of the Gr1^{low}CD11b⁺Ly6C^{high}
175 population in tumors derived from the 4T1-Sca-1⁺ cells, compared to tumors derived from
176 the 4T1-Sca-1⁻ cells (Fig. 2a). Gr1^{high}CD11b⁺Ly6C^{low} cells are immature myeloid
177 progenitors mobilized from the bone marrow by tumor-derived signals capable of
178 establishing an immunosuppressive environment facilitating tumor progression and
179 metastasis^{40,41}. Gr1⁺CD11b⁺ cells form a homogenous population in the circulation
180 (Supplementary Fig. 3a), consistent with the literature⁴², while in the TME they
181 differentiated into two distinct subpopulations, Gr1^{high} and Gr1^{low}. To examine the direct

182 contribution of the tumor-educated Gr1⁺CD11b⁺ cells in promoting the enrichment of the
183 Sca-1⁺ population, we isolated Gr1⁺ cells from primary tumors, bone marrow and spleen of
184 4T1 tumor-bearing BALB/c mice by MACS, and co-cultured them *in vitro* with parental 4T1
185 cells (Fig. 2b). Gr1⁺ cells isolated from tumors (Tu-Gr1⁺CD11b⁺), but not from spleen (Spl-
186 Gr1⁺CD11b⁺) or bone marrow (BM-Gr1⁺CD11b⁺), significantly induced the expansion of a
187 Sca-1⁺ population in 4T1 cells (from 12.5% to 81%, p<0.001) in 48 hours (Fig. 2c). To test
188 whether the expansion of a Sca-1⁺ population from 4T1 cells required direct contact with
189 Tu-Gr1⁺CD11b⁺ or was mediated by soluble factors, we compared the induction in two
190 different co-culture setups, either in standard wells (cell contact) or in Transwells, where
191 Tu-Gr1⁺CD11b⁺ and 4T1 cells were separated by a filter with 0.4 μm pores (Fig. 2d). We
192 did not observe any significant difference in the induction efficiency of Sca-1⁺ populations
193 (measured by flow cytometry) between the two conditions and increasing the 4T1:Tu-
194 Gr1⁺CD11b⁺ cell ratio from 1:1 to 1:3 did not further expand the Sca-1⁺ population (Fig.
195 2e). Furthermore, conditioned medium from co-cultured Tu-Gr1⁺CD11b⁺ and 4T1 cells was
196 also capable of subsequently expanding the Sca-1⁺ population from 4T1 cells alone
197 (Supplementary Fig. 3b). Interestingly, the Tu-Gr1⁺CD11b⁺ induced Sca-1⁺ population
198 appeared more stable in time compared to the isolated 4T1-Sca-1⁺ cells (Supplementary
199 Fig. 3c and Supplementary Fig. 2e). More importantly, when Gr1⁺CD11b⁺ cells-primed 4T1
200 cells were injected into the tail vein, Tu-Gr1⁺CD11b⁺ primed ones showed higher lung
201 colonization capacity compared to Spl-Gr1⁺CD11b⁺ primed one (Fig. 2f-h).

202 These results imply that tumor-educated Gr1⁺CD11b⁺ cells induce the emergence of
203 a highly metastatic Sca-1⁺ population through secreted factors.

204
205 **Tu-Gr1⁺CD11b⁺-induced and tumor-inherent Sca-1⁺ populations display distinct**
206 **gene expression profiles**

207 To unravel the molecular basis for the metastatic capacity of the inherent 4T1- Sca-1⁺
208 population and the Tu-Gr1⁺CD11b⁺ induced Sca-1⁺ population, we first performed
209 transcriptomic profiling of 4T1-Sca-1⁺ and 4T1-Sca-1⁻ cells isolated from the parental 4T1
210 line. Pathway enrichment analysis showed that 4T1-Sca-1⁺ and 4T1-Sca-1⁻ cells
211 expressed different genes associated with distinct signaling pathways (Fig. 3a). The top
212 200 significantly upregulated and downregulated genes were extracted as Sca1 Positive
213 and Sca1 Negative signatures, respectively (Supplementary Table 1). Next, we performed
214 transcriptomic profiling of Tu-Gr1⁺CD11b⁺-primed 4T1, Spl-Gr1⁺CD11b⁺-primed 4T1 and
215 parental 4T1 cells. Pathway enrichment analysis revealed that Tu-Gr1⁺CD11b⁺ and Spl-
216 Gr1⁺CD11b⁺ priming induced distinct transcriptomic alterations in 4T1 cells (Fig. 3b). To
217 focus on the transcriptomic alternations related to the Sca-1⁺ population conversion, we
218 compared Tu-Gr1⁺CD11b⁺-primed vs Spl-Gr1⁺CD11b⁺-primed cells. Interestingly, Tu-
219 Gr1⁺CD11b⁺-primed 4T1 cells expressed both Sca-1 Positive and Sca-1 Negative
220 signatures (Fig. 3c), suggesting that Tu-Gr1⁺CD11b⁺ may twist tumor plasticity by
221 converting the 4T1-Sca-1⁻ cells into 4T1-Sca-1⁺ cells, rather than expanding the pre-
222 existing 4T1-Sca-1⁺ population.

223 To test whether, despite the diverse transcriptional profiles across different Sca-1⁺
224 populations, there could be a common molecular mechanism underlying their induction
225 and metastatic capacity, we compared the significantly differentially expressed genes
226 between 4T1-Sca-1⁺ versus 4T1-Sca-1⁻ and Tu-Gr1⁺CD11b⁺ primed 4T1 versus Spl-
227 Gr1⁺CD11b⁺ primed 4T1 cells. Strikingly, among a total of 1118 up- and 423 down-
228 regulated genes found when comparing the two conditions, only 56 up- and one down-
229 regulated genes were shared (Fig. 3d and Supplementary Table 1). This observation was
230 consistent with the notion that the Sca-1⁺ population in Tu-Gr1⁺CD11b⁺ primed 4T1 cells
231 was different from the inherent 4T1-Sca-1⁺ cells. Nonetheless, the fact that the 4T1-Sca-

232 1⁺ cells and Tu-Gr1⁺CD11b⁺ primed 4T1 cells possessed similar *in vivo* metastatic capacity
233 suggested that among these common pathways some were relevant for 4T1 metastases
234 formation. To this end, we analyzed the publicly available scRNA-seq dataset from 4T1
235 primary tumors of Sebastian et al. ⁴³. In this dataset, several cell types, including cancer
236 cells, epithelial cells, fibroblasts, distinct subpopulations of myeloid cells were identified ⁴³.
237 To determine significant ligand-receptor interactions from the scRNA-seq data, we
238 performed cell-cell interaction analysis with CellPhoneDB ⁴⁴ by focusing on the interactions
239 between epithelial/cancer cells and myeloid cells (Fig. 3e, f). The analysis identified 160
240 ligand-receptor interaction pairs (Supplementary Table 2). Among those pairs, OSM
241 receptor (OSMR) and Pyrimidinergic receptor P2Y6 (P2RY6) were the only ones present
242 inside the 56 common genes shown in Fig. 3d. However, P2RY6 interacts with COPA
243 (Coatomer Complex Subunit Alpha), a membrane protein involved in membrane traffic
244 between endoplasmic reticulum and Golgi ⁴⁵ and, thus, unlikely to mediate cell-cell contact-
245 independent induction of Sca-1⁺ population. As the IL6-JAK-STAT3 signaling pathway was
246 upregulated both in the 4T1-Sca-1⁺ population and Tu-Gr1⁺CD11b⁺-primed 4T1 cells (Fig.
247 3a, b), we next examined the expression of *Osm*, *Osmr*, *Il6st*, *Il6*, and *Il6* receptor (*Il6ra*) in
248 the Sebastian dataset (Fig. 3g). The expression of *Il6* and *Osm* was restricted to myeloid
249 cells, with *Osm* expression being more prominent, similar to a previous report ³³. *Osmr* was
250 predominantly expressed in tumor cells, while *Il6st* and *Il6ra* were homogenously
251 expressed in all cell types.

252 We then explored their expression in the 4T1-Sca-1⁺ cells and Tu-Gr1⁺CD11b⁺
253 primed 4T1 cells. *Osm* and *Il6* expression were very low in all samples (normalized count
254 number less than 7 on average) (Fig. 3h, i), consistent with data in the Sebastian dataset
255 (Fig. 3g). *Osmr* and *Il6ra*, however, were highly expressed in 4T1-Sca-1⁺ cells compared
256 with 4T1-Sca-1⁻ cells, while the expression of *Il6st* was abundant in both populations,

257 though higher in 4T1-Sca-1⁺ cells (Fig. 3h). On the other hand, only *Osmr* was significantly
258 upregulated in Tu-Gr1⁺CD11b⁺ primed 4T1 compared with Spl-Gr1⁺CD11b⁺ primed 4T1
259 (Fig. 3i).

260 Taken together, these results suggest that OSM/OSMR and IL6/IL6R signaling
261 pathways may be involved in the Tu-Gr1⁺CD11b⁺-mediated expansion of 4T1-Sca-1⁺ cells.

262

263 **Tu-Gr1⁺CD11b⁺ cells promote Sca-1⁻ to Sca-1⁺ population conversion**

264 The above results strongly implied that Tu-Gr1⁺CD11b⁺ cells convert Sca-1⁻
265 population into the Sca-1⁺ one. To further test this hypothesis, we compared the cell
266 population dynamics in cultured cells and the orthotopic primary tumor by analyzing
267 publicly available scRNA-seq datasets. By integrating scRNA-seq data from 3D cultured
268 4T1 cells (GSM4812003)⁴⁶ and tumor cells isolated from orthotopically fat pad-injected 4T1
269 primary tumor (PT) (GSM3502134)⁴⁷ (Fig. 4a, b), we observed 5 clusters. Clusters 0, 1, 2,
270 4 were predominant in cultured tumor cells, while cluster 3 was predominant in primary
271 tumors. Single-cell trajectories analysis confirmed that cluster 3 was at the end of the
272 transformation process (Fig. 4c, d). The population dynamics also showed that the fraction
273 of cells in clusters 1, 2 and 4 decreased during the transformation, the one in cluster 0 only
274 minimally increased, while the fraction in cluster 3 massively increased (Fig. 4e).
275 Importantly, very few cultured 4T1 cells expressed *Sca-1* while it was abundantly
276 expressed in the majority of cells in the primary tumor (Supplementary Fig. 4a, upper
277 panel). Consistently, the fraction of cells expressing *Osmr* was higher in the primary tumor
278 compared to cultured cells (Supplementary Fig. 4a, lower panel). Similar observations
279 were obtained when analyzing scRNA-seq data from ER⁺ human breast cancer model
280 MCF-7. After integrating data from cultured MCF-7 cells (GSM4681765) and tumor cells
281 that were isolated from MCF-7 intraductal injected mammary gland (GSM5904917)⁴⁸, 6

282 clusters were identified (Fig. 4f), with clusters 1 and 3 predominant in the cultured MCF-7
283 cells, while clusters 2 and 4 were predominant in the primary tumor (Fig. 4g). Further
284 analysis showed that clusters 2 and 4 expanded during *in vitro* to *in vivo* tumor cell
285 transformation and represented nearly 50% of the *in vivo* primary tumor cells (Fig. 4h-j).
286 Although there is no human homolog of *Sca1* gene, *OSMR* expressing cells were
287 increased upon tumor implantation, especially in clusters 2 and 1 (Supplementary Fig.4b).

288 To further investigate the signals involved in this transformation, we performed
289 GSAE analysis for cluster 3 in 4T1 cells and clusters 2 and 4 in MCF-7 cells, respectively
290 (Fig. 4k-n). By comparing the Hallmark gene signatures, IL6-JAK-STAT3 signature was
291 significantly upregulated in both cell populations (Fig. 4k, m). Interestingly, *Sca1* Positive
292 and *Sca1* Negative signatures were both upregulated (Fig. 4l, n), which is consistent with
293 our *ex vivo* induction experiment (Fig. 3c). To validate the involvement of Tu-Gr1⁺CD11b⁺
294 during the cell population transformation, we extracted the top 50 upregulated genes
295 (Supplementary Table 3) identified by comparing the Tu-Gr1⁺CD11b⁺ with the Sp-
296 Gr1⁺CD11b⁺-stimulated 4T1 cells as Tu-Gr1⁺CD11b⁺ induced signature. Both cell
297 populations predominant in the primary tumor in both 4T1 and MCF-7 models, upregulated
298 the Tu-Gr1⁺CD11b⁺ induced signature (Fig. 4l, n).

299 These data, together with our *in vivo* observations (Fig. 1a-c) and *ex vivo* coculture
300 experiments (Fig. 2b-e and Fig. 3c), indicate that Tu-Gr1⁺CD11b⁺ convert the *Sca1*⁻
301 population to *Sca1*⁺ population, likely, via OSM/IL6 signaling pathway.

302
303 **OSM/IL6-JAK pathway mediates Tu-Gr1⁺CD11b⁺-induced *Sca1*⁺ population**
304 **enrichment**

305 To experimentally interrogate the role of OSM/IL6 in modulating the *Sca1*⁺
306 population, we first measured *Osm* and *Il6* mRNA expression in Spl-Gr1⁺CD11b⁺ and Tu-

307 Gr1⁺CD11b⁺. Indeed, both *Osm* and *Il6* mRNA levels were significantly elevated in Tu-
308 Gr1⁺CD11b⁺ (Fig. 5a). To functionally validate the role of OSM/IL6 in the generation of
309 Sca-1⁺ population, we treated 4T1 cells directly with recombinant OSM and IL6 proteins *in*
310 *vitro* and measured the effect on the Sca-1⁺ population. After 2 days of treatment, both
311 OSM and IL6 significantly increased the frequency of Sca-1⁺ cells from 16% to 38.8% and
312 26.5%, respectively (Fig. 5b). Conversely, blocking OSM and IL6 activities using anti- OSM
313 or -IL6 neutralizing antibodies significantly reduced the emergence of Sca-1⁺ population
314 induced by Tu-Gr1⁺CD11b⁺ conditioned medium (Fig. 5c). The combination of anti-OSM
315 and -IL6 antibodies did not have additive effects suggesting that OSM and IL6 both
316 contribute in promoting Sca-1⁺ population by sharing the same signaling cascades.

317 OSMR and IL6R signal by activating the intracellular Janus tyrosine kinase (JAK)
318 ⁴⁹. To explore the involvement of the JAK pathway in the emergence of the Sca-1⁺
319 population, we treated 4T1 cells with the JAK inhibitor (Ruxolitinib) during exposure to
320 recombinant OSM and IL6. Ruxolitinib treatment prevented the emergence of the Sca-1⁺
321 population in response to recombinant OSM and IL6 (Fig. 5d).

322 From these results, we conclude that OSM/IL6-JAK pathway mediates Tu-
323 Gr1⁺CD11b⁺ -induced Sca-1⁺ population enrichment.

324
325 **Tu-Gr1⁺CD11b⁺-induced Sca-1⁺ population and 4T1-inherent Sca-1⁺ population have**
326 **distinct CSC and EMT gene expression profiles**

327 OSM/IL6-JAK signaling has been reported to support tumor progression by promoting
328 a CSC phenotype and epithelial-mesenchymal plasticity ^{25,36,50}. To further characterize
329 CSC and EMT features in 4T1-Sca-1⁺ cells and Tu-Gr1⁺CD11b⁺ induced Sca-1⁺
330 population, we used our RNAseq data to explore the expression of 17 stem cell and EMT
331 markers (Supplementary Fig. 5). The stem cell markers *Oct4* (*Pou5f1*), *Sox2* and *Nanog*

332 were undetectable or very low in all or some samples. 4T1-Sca-1⁺ cells had higher
333 expression of *Aldh1a1*, *Aldh3a1* and *Podxl* but lower expression of *Klf4* and *Sox9*
334 compared to 4T1-Sca-1⁻ cells. There was no difference in the expression of *Abcg2* and
335 *Has2*. Tu-Gr1⁺CD11b⁺ primed 4T1 cells had higher expression of *Klf4* and *Has2*, lower
336 expression of *Aldh1a1*, *Aldh3a1* and *Sox9*, and similar expression of *Podxl* when
337 compared with Spl-Gr1⁺CD11b⁺ primed 4T1. Among them, only *Has2* expression was
338 specifically elevated in Tu-Gr1⁺CD11b⁺ primed 4T1 compared with control 4T1 and Spl-
339 Gr1⁺CD11b⁺-primed 4T1 (Supplementary Fig. 5a). On the other hand, 4T1-Sca-1⁺ cells
340 had lower expression of *Cdh1* and higher expression of *Snail1*, *Twist1*, *Vim* and *Foxc1*
341 which support an EMT status, although *Zeb1* expression was reduced (Supplementary Fig.
342 5b). Globally, the expression of most of the EMT genes were similar between Tu-
343 Gr1⁺CD11b⁺ and Spl-Gr1⁺CD11b⁺ primed 4T1 cells, except for *Snail2* and *Vim*, whose
344 expression was suppressed in Tu-Gr1⁺CD11b⁺ primed 4T1 (Supplementary Fig. 5b).

345 Taken together, these results indicate that the Tu-Gr1⁺CD11b⁺-induced Sca-1⁺
346 population and inherent Sca-1⁺ population have different CSC and EMT transcriptional
347 profiles, reinforcing the notion that, Tu-Gr1⁺CD11b⁺-induced Sca-1⁺ population are not just
348 enriched tumor-inherent Sca-1⁺ population

349

350 **Chemotherapy enriches a Sca-1⁺ population with CSC features**

351 CSC and cancer cell plasticity contribute to drug resistance in various tumor types,
352 including breast cancer^{51–55}. The above results, including the significantly elevated
353 expression of *Aldh3a1* (a marker of drug resistance) in the 4T1-Sca-1⁺ population
354 prompted us to investigate the resistance of this population to chemotherapy. To this end,
355 we treated 4T1 cells for 48 hours *in vitro* with methotrexate (MTX) and doxorubicin (Dox),
356 two widely used chemotherapy drugs, including in breast cancer. The 48 hours treatment

357 of either drug increased the frequency of Sca-1⁺ population in 4T1 cells (Fig. 6a). Next, we
358 mimicked a clinically relevant situation of cancer cells escaping chemotherapy by exposing
359 4T1 cells to 28 nM MTX, which is slightly higher than the IC₅₀ concentration of the drug
360 (REF!!), for up to 3 weeks and recovered the surviving cells by switching to normal medium
361 (Fig. 6b). The selected cell line, named MR13, was highly enriched in Sca-1⁺ cells (>60%)
362 (Fig. 6c). Compared to parental 4T1 tumor cells, MR13 cells exhibited a higher
363 mammosphere forming efficiency (Fig. 6d), lower *in vitro* proliferative capacity (Fig. 6e),
364 increased survival under non-adhesive conditions (Fig. 6f) and increased cell mobility (Fig.
365 6g), which were consistent with CSC-like properties. When tested in a 48-hours cytotoxicity
366 assay, MR13 cells were more resistant against MTX compared to parental 4T1
367 (Supplementary Fig. 6a).

368

369 **MR13-derived tumors are highly metastatic and rich in Gr1^{high}CD11b⁺ Ly6C^{low} cells**

370 To characterize the *in vivo* behavior of MR13 cells, we orthotopically implanted them
371 into BALB/c mice and monitored the progression. MR13 cells formed smaller primary
372 tumors relative to parental 4T1 cells, that were more metastatic to the lung (Fig. 6h-j) and
373 enriched in Gr1^{high}CD11b⁺ Ly6C^{low} cells compared to 4T1 tumors (Fig. 6k), similarly to 4T1-
374 Sca-1⁺-derived tumors (Fig. 2a). Strikingly, we observed metastases in the heart
375 (Supplementary Fig. 6b), which we never observed with the parental 4T1 cells. MR13 cells
376 retained a large fraction of the Sca-1⁺ population *in vitro*, even when cultured in the
377 absence of MTX (Fig. 6c) and upon *in vivo* expansion (Fig. 6l). Such stability of Sca-1
378 population contrasted with 4T1-Sca-1⁺ cells and Tu-Gr1⁺CD11b⁺-primed 4T1 cells
379 (Supplementary Fig. 2e, g) that, upon isolation or induction reverted to a Sca-1⁻ phenotype,
380 suggesting that MR13 line was capable of self-sustain its own Sca-1⁺ population.

381 Taken together, chemotherapy-selected MR13 cells share some similar *in vivo*
382 characteristics as 4T1-Sca-1⁺ cells, while they are capable of self-sustaining high Sca-1⁺
383 abundancy both *in vitro* and *in vivo*.

384
385 **IL6/IL6R-JAK autocrine signaling maintains Sca-1 positivity and metastatic capacity**
386 **in MR13 cells**

387 To better understand the chemotherapy-induced alterations in MR13 cells, we
388 performed transcriptomic analyses comparing MR13 and parental 4T1 cells. Pathway
389 enrichment analysis showed that the IL6-JAK-STAT3 signature was also elevated in MR13
390 cells (Fig. 7a). Importantly, MR13 gene expression significantly positively correlated with
391 the Sca1 Positive signature. At the same time, it negatively correlated with the Sca1
392 Negative signature (Fig. 7b). This observation suggested that chemotherapy enriched for
393 the inherent 4T1-Sca-1⁺ population, rather than converting plastic Sca-1⁻ cells, as observed
394 upon Tu-Gr1⁺CD11b⁺-stimulation. In addition, *Osmr*, *Il6*, *Il6ra* and *Il6st* were all
395 overexpressed in MR13 cells compared to parental 4T1 cells, while the *Osm* expression
396 was not altered (Fig. 7c). To functionally validate the IL6-JAK signaling pathway in Sca-1⁺
397 population maintenance, we treated MR13 cells with Ruxolitinib *in vitro* for 48 hours. The
398 treatment significantly decreased the fraction of Sca-1⁺ cells (Fig. 7d). Importantly, *in vitro*
399 treatment of MR13 cells with Ruxolitinib for 3 days nearly completely abolished their lung
400 metastatic capacity upon tail vein injection (Fig. 7e-f).

401 Altogether, these data suggest that MR13 cells sustain the metastatic Sca-1⁺
402 population through cell-autonomous activation of the IL6-JAK signaling pathway.

403
404 **Tu-Gr1⁺CD11b⁺ invoked tumor cell signature predicts shorter overall and relapse-**
405 **free survival in breast cancer patients**

406 To evaluate the clinical relevance of the crosstalk between Tu-Gr1⁺CD11b⁺ and tumor
407 cells, we tested whether the Tu-Gr1⁺CD11b⁺-induced 4T1 signature could predict cancer
408 progression in patients. To this end, we interrogated the METABRIC dataset ⁵⁶ with the
409 Tu-Gr1⁺CD11b⁺-induced signature. Thirty-two human orthologue genes (Supplementary
410 Table 3) in the murine 50 genes signature were present in the METABRIC dataset. Patients
411 with the higher expression level of the signature had shorter overall survival (OS; $p =$
412 0.0056) and relapse-free survival (RFS; $p = 0.032$) (Fig. 8a, b). Notably, OSM expression
413 positively correlated with the signature in all patients (Supplementary Fig. 7a), suggesting
414 OSM do contribute to altered signature expression in patients. Of the thirty-two genes, five
415 (*MX1*, *IRF7*, *OAS1*, *CMPK2*, *ISG15*) were commonly discriminant for a shorter OS and
416 RFS (Fig. 8c, d), and taken together, they further enhanced the predictive power (OS:
417 $p=0.00055$; RFS: $p=0.00069$) (Fig. 8e, f).

418 These data indicate that a small set of genes issued from the murine tumor cell
419 signature invoked by Tu-Gr1⁺CD11b⁺ cells can predict a shorter OS and RFS in breast
420 cancer patients, thereby reinforcing the clinical significance of the proposed model.

421

422 **Discussion (1470 words -> 1689 NOW ... OMG)**

423 Metastatic disease and therapy resistance are the leading causes of breast cancer
424 mortality, calling for novel approaches to effectively prevent and cure for metastasis and
425 therapy resistance. This is particularly relevant for TNBC, where in spite of the recent
426 encouraging results with targeted therapies, such as PARP inhibitors for tumors with
427 germline BRCA mutations, or checkpoint inhibitors for PD-L1⁺ tumors, management of
428 metastatic disease remains challenging ⁵⁷⁻⁶⁰. It has been proposed that CSCs present in
429 the primary tumor are responsible for tumor persistence, metastasis, and therapy
430 resistance ^{52,61}. Enrichment and differentiation of CSC contribute to tumor heterogeneity

431 17,19–22. Importantly, CSC features can be intrinsic or plastic and be modulated by cues from
432 the TME^{62–64}.

433 Here, we have interrogated the contribution of the Sca-1⁺ population to breast
434 cancer metastasis and its modulation by the TME. We reported that tumor-educated
435 Gr1⁺CD11b⁺ cells (Tu-Gr1⁺CD11b⁺) instigate cancer metastasis by twisting cancer cell
436 plasticity and enriching for a Sca-1⁺ population, with enhanced metastatic capacity. We
437 identified OSM/IL6-JAK as a paracrine communication axis between Tu-Gr1⁺CD11b⁺ and
438 breast cancer cells and as an autocrine loop in chemotherapy-resistant tumor cells,
439 promoting tumor heterogeneity, CSC features and metastatic capacity. Importantly, breast
440 cancer patients expressing high levels of the human orthologues of the gene expression
441 signatures invoked by Tu-Gr1⁺CD11b⁺ have significantly shorter OS and RFS, reinforcing
442 the clinical significance of our findings. While some of these elements have been reported
443 individually before, our results extend these observations by providing an integrative view
444 of paracrine (Tu-Gr1⁺CD11b⁺-induced) and autocrine (chemotherapy-induced)
445 communication in regulating tumor heterogeneity, cancer cell plasticity, metastasis, and
446 resistance to chemotherapy.

447 A main observation stemming from this study is that Sca-1⁺ population exists under
448 three different conditions: as inherent 4T1-Sca-1⁺ population, upon exposure to Tu-
449 Gr1⁺CD11b⁺ cells and upon chemotherapy treatment (MR13). All these populations had
450 higher metastatic ability compared to their counterpart controls. GSEA analysis
451 suggested that the Tu-Gr1⁺CD11b⁺-induced Sca-1⁺ population was likely to convert from
452 the Sca-1⁻ population (Fig. 3c and Fig. 4), while the Sca-1⁺ population surviving
453 chemotherapy (MR13) appeared to be enriched from an inherent Sca-1⁺ population (Fig.
454 7b). In addition, the different gene expression signature of Tu-Gr1⁺CD11b⁺-induced Sca-
455 1⁺ population relative to the inherent Sca-1⁺ cells suggest a remarkable functional

456 plasticity of these cells. This plasticity is further supported by comparing single cell gene
457 expression of murine 4T1 and human MCF-7 breast cancer cells, using publicly available
458 scRNA-seq datasets, before and after *in vivo* growth (Fig. 4). *In vivo*, tumor cells undergo
459 a transformation enriching for Sca-1 (in the mouse), OSMR expressing cells, Sca1
460 Positive, Sca1 Negative and Tu-Gr1⁺CD11b⁺-induced signatures, and IL6-JAK signaling
461 pathway from precursor cells (Sca-1⁻ in the mouse) (Fig. 4). Gong *et al.* have reported
462 that sorted Sca-1⁻ 4T1 cells could be transiently transformed into a Sca-1⁺ population by
463 radiotherapy⁶⁵. An analogous observation was reported in colorectal cancer, where
464 selective ablation of LGR5⁺ CSCs in organoids leads to initial tumor regression, followed
465 by regrowth driven by LGR5⁺ CSCs reemerging from the LGR5⁻ population⁶⁶. Taken
466 together, our observations further consolidate the notion that cancer consists of a
467 heterogenous and plastic tumor mass, including highly metastatic cell populations, by
468 demonstrating that tumor recruited and educated Gr1⁺CD11b⁺ cells contribute to such
469 plasticity by inducing the conversion of low metastatic Sca-1⁻ population into a highly
470 metastatic Sca-1⁺ population. Dedicated time course scRNA-seq analyses together with
471 lineage tracing experiments may help to further characterize the detailed origin,
472 development, fate, and function of these Sca-1⁺ populations during cancer progression.

473 Recruitment and accumulation of Gr1⁺CD11b⁺ cells in the TME, particularly through
474 the chemokines CCL2, CXCL1 and CXCL2, or IL-33, is considered a critical step for their
475 contribution to tumor progression and metastasis⁶⁷⁻⁷⁰. Consistent with these observations,
476 tumors derived from sorted 4T1-Sca-1⁺ cells, or MR13 cells that are intrinsically enriched
477 for Sca-1⁺ cells, have a higher content of Gr1^{high}CD11b⁺Ly6C^{low} cells compared to tumors
478 derived from 4T1-Sca-1⁻ or parental 4T1 cells, respectively (Fig. 2a and 5k). Beyond
479 recruitment, tumor-mediated education of Gr1⁺CD11b⁺ cells appears to be necessary to
480 gain higher metastatic activity: Only Gr1⁺CD11b⁺ cells recovered from primary tumors (but

481 not from spleen or bone marrow) induced Sca-1 positivity and enhanced metastatic ability
482 in 4T1 cells (Fig. 2c, e). The role of Gr1⁺CD11b⁺ cells in promoting metastasis has been
483 mainly attributed to promotion of angiogenesis, EMT and immunosuppression^{17,68}. Peng
484 *et al.*, reported the ability of those cells to endow CSC-like features to breast cancer cells
485 but their metastatic capacity was not interrogated¹⁷. Our observations suggest a self-
486 sustaining positive feedback mechanism between highly metastatic cancer cells (Sca-1⁺
487 population) and Gr1⁺CD11b⁺ cells: inherent Sca1⁺ CSC-like, metastatic, cells promote
488 recruitment and local education of Gr1⁺CD11b⁺ cells, which in turn promote tumor
489 heterogeneity, cancer cell plasticity and metastatic capacity by converting low-metastatic
490 Sca1⁻ cells into additional high-metastatic Sca1⁺ cells (Fig. 9).. Recently, it was reported
491 that neutrophils escorting blood circulating tumor cells (CTCs) expands the metastatic
492 potential of CTCs⁷¹. While this effect was attributed to the promotion of cell cycle
493 progression of CTCs through direct contact with the neutrophils, in light of our findings, one
494 may also consider the possibility that clustered neutrophils may also promote the
495 expansion of a CSCs-like phenotype with higher metastatic capacity. Interestingly, OSM
496 was reported to be expressed by neutrophils cocultured with breast cancer cells³⁶ and to
497 promote phenotypic changes associated with mesenchymal and stem cell-like
498 differentiation in breast cancer^{36,72}. Together with our observation, these findings further
499 reinforce the notion that boosting the *Osm* expression in Gr1⁺CD11b⁺ cells is part of their
500 educating program prompted by the tumor. One outstanding question raised by these
501 observations is by which mechanisms and pathways cancer cells, in particular Sca-1⁺
502 ones, educate Gr1⁺CD11b⁺ cells to acquire cancer plasticity-promoting activity.

503 Besides directly activating tumor cells, OSM has also been shown to remodel
504 macrophages and fibroblasts of the TME^{33,36}. Araujo *et al.* recently reported that OSM
505 derived from tumor-infiltrating myeloid cells reprogram fibroblasts to secrete VEGF and the

506 chemokines CXCL1 and CXCL16, resulting in enhanced myeloid cell recruitment and
507 breast cancer progression ³³. Here we extend these observations by demonstrating that
508 tumor-educated Gr1⁺CD11b⁺-derived OSM/IL6 twist cancer cell plasticity by promoting a
509 rapid but reversible conversion of Sca-1⁻ cells into more metastatic Sca-1⁺ cells (Fig. 5b).
510 We further broaden the implications of the OSM/IL6-JAK axis, by demonstrating that MR13
511 cells that have escaped chemotherapy hijacked this paracrine mechanism in a cell
512 autonomous manner by elevating the *Il6* expression (Fig. 9). Significantly, a short *in vitro*
513 treatment with Ruxolitinib effectively abrogated their metastatic capacity (Fig. 7e, f).

514 While OSM/OSMR is the only interaction pair identified by the cell-cell interaction
515 analysis (Fig. 3f, g), it is possible that other molecular mechanisms may also play roles in
516 modulating Sca-1⁺ cell plasticity and metastasis. One candidate is the IL6/IL6R
517 communication axis, which was less prominent in the cell-cell communication analysis (Fig.
518 3f, g), but was highly expressed in our experimental data in Tu-Gr1⁺CD11b⁺ compared with
519 Spl-Gr1⁺CD11b⁺ (Fig. 5a), and in chemotherapy-resistant MR13 cells compared with 4T1
520 (Fig. 7c). Moreover, the neutralization of IL6 also suppressed the Tu-Gr1⁺CD11b⁺
521 conditioned medium induced Sca-1⁺ cell enrichment, much alike OSM inhibition (Fig. 5c).

522 Importantly, we demonstrated that a human orthologue signature of the 4T1 gene
523 expression signature invoked by Tu-Gr1⁺CD11b⁺ can predict a significantly shorter OS and
524 RFS in breast cancer patients (Fig. 8). This finding strengthens the clinical significance of
525 the observed crosstalk between Tu-Gr1⁺CD11b⁺ and tumor cells. Strikingly, the five genes
526 that significantly contribute to the discriminatory power of the signature are genes related
527 to native or viral immunity or regulated by interferon. While expression of interferons and
528 interferon response genes in breast cancer has been mainly associated with tumor
529 suppression and improved survival ⁷³, there is evidence also correlating interferon
530 responses with tumor promotion, therapy resistance and reduced survival ⁷⁴. As

531 JAKs/STATS are activated by both IFN and OSM/IL6 receptors, it is conceivable that
532 OSM/IL6 only activates a subset of the IFN-induced genes with tumor-promoting activity,
533 as the case for Mx1⁷⁵. Consistent with our findings, JAK/STAT signaling has recently been
534 shown to initiate the lineage plasticity in prostate cancer as well as to promote lineage
535 plasticity-driven targeted therapy resistance in a stem-like subpopulation of prostate cancer
536 ^{76,77}. On the other hand, Aouad *et al.* showed that epithelial-mesenchymal plasticity is
537 essential for the generation of a dormant cell state of ER⁺ breast cancer during progression,
538 and the activation of IL6-JAK-STAT signaling triggers tumor cell awakening and recurrence
539 ⁴⁸.

540 One crucial question raised by these results is whether the OSM/IL6-JAK pathway is
541 a potential actionable clinical target to impinge on metastatic progression and therapy
542 resistance. In particular, the observation that a short *in vitro* treatment of the highly
543 metastatic MR13 cells profoundly suppressed their metastatic capacity *in vivo* (Fig. 7e, f),
544 suggests potential long-lasting effects consistent with an adjuvant effect. JAK inhibitors are
545 being tested in clinical trials in breast cancer. A phase I study combining Ruxolitinib with
546 paclitaxel in HER2-negative metastatic breast cancer showed good tolerability and
547 evidence of activity ⁷⁸. A phase I/II trial of Ruxolitinib in combination with trastuzumab in
548 metastatic HER2 positive breast cancer and a phase II study combining Ruxolitinib with
549 capecitabine in advanced HER2⁻ breast cancer, however, did not improve progression-free
550 survival ^{79,80}. The absence of benefits in these studies in advanced breast cancer and our
551 reported mechanistic observations on metastatic progression, raise the question of
552 whether the JAK inhibitors should be considered in adjuvant setting in high-risk patients,
553 to prevent progression to metastases, rather than treating patients already bearing
554 metastases.

555 In conclusion, we reported here that a subpopulation of tumor cells within the tumor

556 mass educates required Gr1⁺CD11b⁺ cells to convert a low metastatic subpopulation into
557 highly metastatic one, through the OSM/IL6-JAK signaling axis (Fig. 9). The clinical
558 relevance of this observation is supported by human transcriptomic data. This process is
559 hijacked by tumor cells that survived chemotherapy and evolved toward a highly metastatic
560 phenotype via cell autonomous IL6-JAK signaling. Importantly, a short *in vitro* treatment
561 with a clinically approved JAK inhibitor, Ruxolitinib, suppresses their metastatic capacity
562 these cells *in vivo*. These results should stimulate considering testing JAK inhibitors in the
563 adjuvant setting in TNBC breast cancer patients at high-risk for metastatic progression.

564

565

566 **Methods**

567 **Cell culture.** The 4T1 murine breast cancer cell line was kindly provided by Dr Fred R.
568 Miller (Michigan Cancer Foundation, Detroit, MI, USA). 4T1 cells were cultured in high
569 glucose DMEM supplemented with 10% heat-inactivated FBS, 1% penicillin–streptomycin
570 (P/S, from Gibco) and 1% Non-Essential Amino Acid (Gibco).

571

572 **Tumor models.** 4T1, MR13, sorted 4T1-Sca-1⁺ and 4T1-Sca-1⁻ (5x10⁴ cells in 50µl
573 PBS/10% of 8.1 mg/ml Matrigel Matrix, were injected in the fourth right mammary gland of
574 mice. Prior to surgery, ketamine (1.5 mg/kg) and xylazine (150 mg/kg) (both from Graeub)
575 were injected intra-peritoneally to anesthetize the animals. Immune cell populations were
576 analyzed at different time points post-tumor cell injection. Tumor length and width were
577 measured twice a week with caliper and used to calculate tumor volume by the following
578 equation: volume = (length x width²) x π/6. Tumors were collected and weighted at
579 necropsy. For the intravenous injections, 2x10⁵ sorted 4T1-Sca-1⁺ and 4T1- Sca-1⁻ tumor
580 cells resuspended in a volume of 50 µl of PBS were injected into the mice tail vein. Lung

581 metastases were quantified 10 days post-injection. At each indicated time point, mice were
582 sacrificed according to defined ethical criteria and were killed by CO₂ inhalation followed
583 by neck dislocation or terminal bleeding. All animal procedures were performed in
584 accordance with the Swiss legislations on animal experimentation and approved by the
585 Cantonal Veterinary Service of the Cantons Vaud and Fribourg for experiments in
586 Lausanne and Fribourg (VD_1486.2; 2017_34_FR; 2017_34_FR, 2014_58_FR; 2011-33-
587 FR).

588
589 **Reagents and chemicals.** Growth factor reduced Matrigel Matrix (MG) was obtained from
590 Becton Dickinson (BD Biosciences). Collagenase I was purchased from Worthington and
591 DNase I from Roche. Bovine serum albumin (BSA), crystal violet (CV) and
592 paraformaldehyde (PFA) were obtained from Sigma-Aldrich. Drugs, inhibitors and
593 cytokines: Doxorubicin and Methotrexate (generously provided by the Department of
594 Oncology, University Hospital, University of Lausanne, Lausanne, Switzerland),
595 Ruxolitinib (JAK inhibitor, Cat N°7064, Biotechne), anti-mouse Oncostatin M (R&D
596 systems), anti-mouse IL-6 (BioXCell), recombinant mouse Oncostatin M and IL-6
597 (Biolegend, Cat #: 762802 & 575702 respectively).

598
599 **Antibodies.** The following anti-mouse antibodies were used following manufacturer's
600 instructions: anti-CD16/CD32 Fc blocking antibody (BD Biosciences), anti-CD24-FITC
601 (clone M1/69, eBioscience), anti-CD29-PE and-PE-Cy5 (clone HMβ1-1, BioLegend), anti-
602 Sca-1-APC (clone D7, eBioscience), anti-CD61-Alexa 647 (clone 2C9.62(HMβ3-1),
603 BioLegend, anti-CD45-PE (clone 30-F11, BD Biosciences), anti-Gr1-eFlour450 (clone
604 RB6-8C5,eBioscience), anti-Ly6C FITC (clone HK1.4, BioLegend), anti-Ly6G-APC (clone
605 1A8-Ly6g,eBioscience), anti-F4/80 PerCP/Cy5 (clone BM8, eBioscience), anti-CD11b-PE-

606 Cy7 (clone M1/70, eBioscience), anti-CD11c-APC-eFluor780 (clone N418, eBioscience),
607 anti-CD4-FITC (clone 6K1.5, eBioscience), anti-CD8-PE (clone 53-6.7, eBioscience), anti-
608 B220-APC (clone RA3-6B2, eBioscience), anti-CD49b-eFlour450 (clone DX5, BioLegend),
609 Annexin V-APC (clone B217656, BioLegend), Propidium Iodide-PerCP (Clone V13245,
610 Life technologies).

611
612 **Magnetic cell sorting (MACS).** MACS separators were used for positive and negative cell
613 selections based on manufacturer's instructions. Briefly, cells were counted and resuspend
614 in 500 μ l of MACS buffer with 10 μ l of fluorescent coupled antibody of interest (APC-
615 conjugated anti-Sca-1 and PE-conjugated anti-Gr1) per 10^7 cells added. Cells were
616 incubated for 30 minutes in the dark at 4°C and then washed with MACS buffer. After
617 centrifugation and resuspension in 80 μ l of MACS buffer per 10^7 cells, 20 μ l of anti- APC-
618 conjugated magnetic beads (Miltenyi Biotec) per 10^7 cells was added. After a 20 minutes
619 incubation in the dark at 4°C, cells were washed with MACS buffer. After the centrifugation
620 they were resuspended in MACS buffer and the magnetic separation was performed using
621 LS MACS column (maximum 10^8 labeled cells) for positive selection and LD MACS column
622 (maximum 10^8 labeled cells) for negative selection (Miltenyi Biotec). The purity of positive
623 subpopulation was >70% and <99% for the negative subpopulation.

624
625 **Co-culture of Gr1⁺CD11b⁺ cells sorted from tumors or spleen of 4T1 tumor bearing**
626 **mice.** Gr1⁺ cells were sorted from tumors or spleen at day 23 post-injection (see below
627 Magnetic beads cell sorting section). Afterwards, 1.5×10^5 4T1 cells were co-cultured in 6
628 wells plates using Transwell plates (0.4 μ m, Nunc, ThermoFisher Scientific) with
629 Gr1⁺CD11b⁺ sorted cells (top) and 4T1 cells (bottom) at different 4T1: Gr1⁺CD11b⁺ ratios

630 (1:1, 1:3 and 1:5). After 48 hours of co-culture, cells were analyzed for Sca-1 expression
631 and gene expression by flow cytometry and semi-quantitative real-time qPCR as indicated.

632
633 **Flow cytometry analysis on tissue samples.** Mice were sacrificed at different time points
634 for blood and tumors collection. Tumors were cut in small pieces with scissors, washed,
635 and digested in serum free medium supplemented with Collagenase I and DNase I
636 (Roche). The mixture was incubated at 37 °C for 45 minutes on a shaking platform.
637 Subsequently, serum-supplemented medium was added to neutralize the enzymatic
638 reaction and the tissue suspensions were filtered through a 100 µm and a 70 µm sterile
639 nylon gauzes. Upon centrifugation (5 minutes at 1400 rpm), pellets were recovered and
640 red blood cells lysed with ACK buffer (Biolegend). The staining procedure and the flow
641 cytometry acquisition are as described previously⁸¹. Data acquisition was performed using
642 the FACSCalibur (BD Biosciences) or MACSQuant flow cytometer from Miltenyi Biotec and
643 data analyzed by FlowJo v10.0.7 (tree Stat Inc.).

644
645 ***In vitro* cell proliferation assay.** Cells were collected and seeded in tissue culture 96-
646 wells-plates (Costar) at 3'000 cells/well. Cells were grown in complete medium for 24, 36,
647 72 and 96 hours. At each time point cells were washed once with PBS, then fixed with 4%
648 PFA and stained with 0.5% crystal violet solution for 0.5 hours. The stained cells were
649 gently washed with deionized water to remove the extra dye and air-dried overnight at
650 room temperature. After solubilizing the dye with crystal violet eluting buffer (70% ethanol
651 and 1% acetic acid), cell viability was assessed by reading the absorbance at 595 nm
652 wavelength in a multiwell plate reader (Modulus II microplate reader, Turner Biosystems).
653 Results were analyzed by Prism (Graph pad software, Inc.) expressed as mean values of
654 optical density (OD) of octuplet determinations ± SEM.

655
656 ***In vitro* cytotoxic assay.** Tumor cells were plated at a concentration of 3'000 cell/well into
657 96-wells plates. The following day, a series of concentrations of the different drugs were
658 supplemented to the culture medium. Untreated control cells were kept in normal culture
659 medium. Cell viability of each well was assessed with crystal violet staining 48 hours after
660 treatment, as described above. Results were analyzed by Prism software by a non-linear
661 regression analysis and expressed as relative cell viability compared with non-treated
662 control. The 50% maximum inhibition concentrations (IC₅₀) were used to determine the
663 drug-resistant ability of treated cells.

664
665 **Real-time reverse transcription qPCR and primers.** Changes in mRNA expression
666 levels were determined by semi-quantitative real-time qPCR. RNA samples were obtained
667 from adherent cells using RNeasy kit from QIAGEN according to manufacturer's
668 instructions. From each sample, 1 µg RNA was retro-transcribed using SuperScript II
669 Reverse Transcriptase kit (Life Technologies – Invitrogen), according to manufacturer's
670 instructions. The reactions were performed in a StepOnePlus™ thermocycler (Applied
671 Biosystems, Life Technologies – Invitrogen) using the KapaSYBR® FAST SYBR Green
672 Master Mix (Kapa Biosystems). Each reaction was performed in triplicates and values were
673 normalized to murine 36B4 housekeeping gene. The comparative C_t method was used to
674 calculate the difference of gene expression between samples. The following murine-
675 specific primers (Microsynth AG) were used:

676 Sca-1 (F:5'-TCAGGAGGCAGCAGTTATTGTG-3',R: 5'-TGGCAACAGGAAGTCTTCACG-
677 3'), 36B4(F:5'-GTGTGTCTGCAGATCGGGTAC-3',R:5'-CAGATGGATCAGCCAGGAAG-
678 3'), OSM (F: 5'- ATGCAGACACGGCTTCTAAGA-3', R: 5'- TTGGAGCAGCCACGATTG
679 G-3'), OSMR: (F: 5'- CATCCCGAAGCGAAGTCTTGG-3', R: 5'-

680 GGCTGGGACAGTCCATTC TAAA-3'), IL-6: (F: 5'- TACCACTTCACAAGTCGGAGGC-3',
681 R: 5'- CTGCAAGTGCATCAT CGTTGTTC-3').

682

683 **Histopathology.** Tumors and lungs were harvested at the end of the experiments, fixed in
684 formalin and embedded in paraffin. 5 µm thick serial sections were cut from the tissue
685 blocks. 3-4 sections taken at 100 µm distance were stained with hematoxylin and eosin
686 (H&E) and used to assess tumor morphology and quantify lung metastasis. Slides were
687 scanned by Nanozoomer (Hamamatsu Photonics) and metastasis were counted manually
688 using NDP.viewer2 software (Hamamatsu Photonics). Metastatic index was calculated by
689 normalizing the metastasis number with the volume of primary tumor.

690

691 **Anoikis assay.** A 6 wells plate was coated with 500 µl of 3% Poly (2-hydroxyethyl
692 methacrylate) (poly-HEMA) (Sigma-Aldrich) dissolved in 95% ethanol overnight. Wells
693 without poly-HEMA served as control. The day after, 2×10^5 cells resuspended in DMEM
694 medium were seeded. The plate was incubated at 37°C for 24 hours. Cells were collected,
695 centrifuged and resuspended in 100 µl of 1x -binding buffer (1 ml of 5x annexin-binding
696 buffer (Life Technologies, Invitrogen) in 4 ml of deionized water). 3 µl APC annexin V
697 (BioLegend) and 1 µl of 100 µg/ml Propidium Iodide (PI) working solution (5 µl of 1mg/ml
698 PI stock, Life Technologies, Invitrogen) in 45 µl of 1x annexin-binding buffer) were added
699 to each 100 µl cell suspension. Cells were incubated for 15 minutes at room temperature
700 protected from light. 200 µl of 1x annexin V-binding buffer was added to the cells and
701 samples were kept on ice. Apoptotic (Annexin V^{pos} and PI^{neg}) and dead (PI^{pos}) cells were
702 analyzed by flow cytometry. Results were expressed as percentage of dead cells ± SEM.

703

704 **Mammosphere-forming assay** 5'000 cells/well were seeded in non-adhesive U bottom
705 96-wells plate in a semi-solid MEGM medium supplemented with 20 ng/ml EGF, and 20
706 ng/ml bFGF and heparin. Medium was gently replaced every 3 to 4 days. After 11 to 14
707 days culture, mammospheres of 50 to 150 μm diameter were detected under the
708 microscope (bright field) and counted to quantify the sphere formation efficiency (SFE) as
709 percentage of the initial number of seeded cells per well.

710
711 **Bulk RNA sequencing and data analysis.** Four independent sorts of 4T1-Sca-1⁺ and
712 4T1-Sca-1⁻ cells (as described in the magnetic cell sorting section) or four independent 4T1
713 cells primed with Tu- Gr1⁺CD11b⁺ or Spl-Gr1⁺CD11b⁺ were prepared. RNAs of these cells
714 were isolated using the NucleoSpin RNA protocol of Macherey-Nagel (as described in real-
715 time (RT) qPCR and primers section). Samples were normalized for 1 μg RNA in a volume
716 of 20 μl , sequenced on the NextSeq500 sequencer using the NextSeq 500/550 HT reagent
717 v2 kit (Illumina) at the Swiss Integrative Center for Human Health (SICHH) in Fribourg, or
718 the Lausanne Genomics Technologies Facility (GTF, UNIL) in Lausanne, Switzerland. For
719 data analysis, all sequencing reads were processed for quality control, removal of low
720 quality reads, adaptor sequence and ribosomal RNA by fastqc (0.11.8)⁸², multiqc (1.9)⁸³,
721 Trimmomatic (0.39)⁸⁴ and SortMeRNA(2.1)⁸⁵ accordingly. The filtered reads were mapped
722 to the reference genome (mm10) using htseq-count (0.6.1)⁸⁶ or Salmon (0.99.0)⁸⁷. The
723 normalization of the read counts and the analysis of the differential expression between
724 the groups of samples were performed with in R(v4.1.3), a free software environment
725 available at <https://www.r-project.org/> using packages DESeq2 (v3.15)⁸⁹. Pathway
726 enrichment analysis was performed using packages GSVA(1.42.0)⁹⁰ and
727 GSEABase(1.56.0)⁹¹ with the input of DESeq2 normalized count numbers using ssgsea
728 method comparing the Hallmark genesets from MSigDB (v7.4.1)⁹² with default settings.

729 The significant altered pathways were determined by computing moderated t-statistics and
730 false discovery rates with the `limma(3.50.3)`⁹³ for pair-wised comparison. The heatmaps
731 were produced with R package `pheatmap(1.0.12)`⁹⁴ with default settings while pathway
732 hierarchy clustering was performed by similarity based on Euclidean distance and the ward
733 aggregation algorithm. The Sca1 Positive and Sca1 Negative signatures were extracted
734 from the top 200 most upregulated or downregulated genes in 4T1-Sca-1⁺ and 4T1-Sca-1⁻
735 RNAseq data, respectively, with the threshold of adjusted p-value <0.05, fold change >1.5
736 or <-1.5 and average normalized count number >20. For Venn diagram, the genes fulfilling
737 the threshold of adjusted p-value < 0.05, fold change > 1.5 or < -1.5 and average
738 normalized count number >20 are compared. The figures were produced with R package
739 `venn (1.10)`⁹⁵. Further analysis and figures generation were performed in R using
740 packages `tidyverse(1.3.1)`⁹⁶, `ggplot2(3.3.6)`⁹⁷, `circlize(0.4.15)`⁹⁸, `biomaRt(2.50.3)`^{99,100},
741 `RColorBrewer (1.1-3)`¹⁰¹, `clusterProfiler (4.2.2)`^{102,103}, `enrichplot (1.14.2)`¹⁰⁴, `ggpubr(`
742 `v0.4.0)`¹⁰⁵ `ggbreak (0.1.0)`¹⁰⁵.

743
744 **Microarray hybridization and data analysis** Experiments were performed as previously
745 described¹⁰⁶. Briefly, triplicates wells of cultured 4T1 and MR13 cells were used for RNA
746 extraction using RNeasy kit (QIAGEN). Probe synthesis and GeneChip Mouse Gene Exon
747 1.0 ST Array (Affymetrix Ltd) hybridization were performed at the GTF, UNIL, Lausanne,
748 Switzerland. Microarray analyses were carried out with R. After quantification of gene
749 expression with robust multi-array normalization¹⁰⁰ using the BioConductor package `Affy`,
750 (<http://www.bioconductor.org/>) significance of differential gene expression was determined
751 by computing moderated t-statistics and false discovery rates with the `limma` package⁹³.
752 Annotation was based on the genome version NCBI Build 36 (Feb. 2006). The obtained p-
753 values were corrected for multiple testing by calculating estimated false discovery rates

754 (FDR) using the method of Benjamini-Hochberg. Heatmaps were produced by color-coding
755 gene-wise standardized log gene expression levels (mean zero standard deviation one).
756 Probe-sets were shown hierarchically clustered by similarity based on Euclidean distance
757 and the ward aggregation algorithm.

758
759 **Public RNAseq data analysis** The RPKM normalized gene expression data in Ross
760 dataset (GSE150928) from multiple murine models of breast cancer metastasis was
761 obtained from Gene Expression Omnibus (GEO) in the NCBI data repository. The data
762 were analyzed and plot with R package tidyverse(1.3.1)⁹⁶, ggplot2 (3.3.6)⁹⁷ and ggpubr
763 (v0.4.0)¹⁰⁷. The single-cell RNAseq data in Sebastian dataset⁴³ was obtained from Dryad
764 data repository (<https://doi.org/10.6071/M3238R>). The data were analyzed with R package
765 Seurat (3.0)¹⁰⁸. The tumor and different myeloid cell populations were extracted for cell-
766 cell interaction analysis using CellPhonDB (2.0)⁴⁴. The identified interaction pairs were
767 extracted and plot using circlize (0.4.15)⁹⁸ and ComplexHeatmap (2.11.2)¹⁰⁹. The ligands
768 and receptors annotated in the circular plot were compiled from databases in
769 CellTalkDB¹¹⁰, SingleCellSignalR¹¹¹. To investigate the tumor cell dynamics, datasets for
770 4T1 (GSE158844 and GSM3502134) and MCF-7 (GSM4681765 and GSM5904917) were
771 obtained from GEO. The data were filtered and normalized separately before merging with
772 IntegrateData function included in Seurat. Cell cycle regression was performed according
773 to the standard protocol of Seurat. For MCF-7, due the huge difference of the sample size,
774 2000 cells were randomly selected from GSM4681765 data, and then merged with
775 GSM5904917. Single-cell trajectories analysis was performed with monocle 3¹¹²⁻¹¹⁵ with
776 default settings and the root and start point were selected manually for pseudotime
777 calculation. The GSEA analysis of selected clusters was performed with R package
778 fgsea¹¹⁶ and the gene rank was calculated with Wilcoxon rank sum test and auROC

779 analysis using wilcoxauc function included in presto package. The Tu-Gr1⁺CD11b⁺-
780 induced signature was extracted by comparing gene expression between Tu-Gr1⁺CD11b⁺
781 and Spl-Gr1⁺CD11b⁺-educated 4T1 cells with adjusted p-value <0.05, fold change >2, and
782 the top 50 genes were selected.

783
784 **Clinical data analysis.** To validate our finding in clinical data, the human orthologs of
785 murine Tu-Gr1⁺CD11b⁺-induced signature genes were used. Conversion from murine to
786 human gene symbols and Entrez IDs was performed with the biomaRt package (2.46.3)
787 ^{99,100}, using the reference mart <https://dec2021.archive.ensembl.org>. Molecular Taxonomy
788 of Breast Cancer International Consortium (METABRIC) breast cancer data was
789 downloaded from cBioPortal ^{117–119} in August 2022, and expression data was log2
790 transformed. Expression values were stratified in two groups by median values. Survival
791 curves were generated using the ggsvplot function from the survminer package
792 (0.4.9)¹⁰⁷, and were compared between groups using a log-rank test. Survival curves were
793 created using the survfit function from the survival package (3.2.11) ¹²⁰. Cox proportional
794 hazard regression model was performed through the coxph function of the same package.

795 **Statistical analyses.** Unless specified, the data were presented as mean ± SEM from at
796 least 3 independent experiments, unless otherwise indicated. Statistical comparisons
797 were performed by an unpaired Student's t test with a two-tailed distribution or one-way
798 ANOVA analysis of variance with Bonferroni post-test, using Prism 7.0 GraphPad
799 Software, Inc.

800

801 **Graphic illustrations.** Illustrative schemes were created with BioRender.com.

802

803 **Data and code availability**

804 The raw and processed bulk RNAseq data used to generate figures in Fig. 3 and
805 Supplementary Fig. 5 and microarray data used to generate figures in Fig. 7 have been
806 deposited in the GEO database under the access code GSEXXXXXX.

807 The code used for the analyses is open-source and available through with R packages
808 described in methods.

809

810 **References**

- 811 1. Fares, J., Fares, M. Y., Khachfe, H. H., Salhab, H. A. & Fares, Y. Molecular
812 principles of metastasis: a hallmark of cancer revisited. *Signal Transduct. Target. Ther.* **5**,
813 1–17 (2020).
- 814 2. Valdés-Mora, F. *et al.* Single-cell transcriptomics reveals involution mimicry during
815 the specification of the basal breast cancer subtype. *Cell Rep.* **35**, 108945 (2021).
- 816 3. Yang, D. *et al.* Lineage tracing reveals the phylodynamics, plasticity, and paths of
817 tumor evolution. *Cell* **185**, 1905-1923.e25 (2022).
- 818 4. Torborg, S. R., Li, Z., Chan, J. E. & Tammela, T. Cellular and molecular
819 mechanisms of plasticity in cancer. *Trends Cancer* **8**, 735–746 (2022).
- 820 5. Baccelli, I. & Trumpp, A. The evolving concept of cancer and metastasis stem
821 cells. *J. Cell Biol.* **198**, 281–293 (2012).
- 822 6. Lawson, D. A., Kessenbrock, K., Davis, R. T., Pervolarakis, N. & Werb, Z. Tumour
823 heterogeneity and metastasis at single-cell resolution. *Nat. Cell Biol.* **20**, 1349–1360
824 (2018).
- 825 7. Celià-Terrassa, T. & Jolly, M. K. Cancer Stem Cells and Epithelial-to-
826 Mesenchymal Transition in Cancer Metastasis. *Cold Spring Harb. Perspect. Med.* **10**,
827 a036905 (2020).
- 828 8. Dagogo-Jack, I. & Shaw, A. T. Tumour heterogeneity and resistance to cancer
829 therapies. *Nat. Rev. Clin. Oncol.* **15**, 81–94 (2018).
- 830 9. McDonald, K.-A. *et al.* Tumor Heterogeneity Correlates with Less Immune
831 Response and Worse Survival in Breast Cancer Patients. *Ann. Surg. Oncol.* **26**, 2191–
832 2199 (2019).
- 833 10. Hata, A. N. *et al.* Tumor cells can follow distinct evolutionary paths to become
834 resistant to epidermal growth factor receptor inhibition. *Nat. Med.* **22**, 262–269 (2016).

- 835 11. Ramirez, M. *et al.* Diverse drug-resistance mechanisms can emerge from drug-
836 tolerant cancer persister cells. *Nat. Commun.* **7**, 10690 (2016).
- 837 12. Oskarsson, T., Batlle, E. & Massagué, J. Metastatic stem cells: sources, niches,
838 and vital pathways. *Cell Stem Cell* **14**, 306–321 (2014).
- 839 13. Ye, F. *et al.* CD49f Can Act as a Biomarker for Local or Distant Recurrence in
840 Breast Cancer. *J. Breast Cancer* **20**, 142–149 (2017).
- 841 14. Vaillant, F. *et al.* The Mammary Progenitor Marker CD61/ β 3 Integrin Identifies
842 Cancer Stem Cells in Mouse Models of Mammary Tumorigenesis. *Cancer Res.* **68**,
843 7711–7717 (2008).
- 844 15. Li, J. J., Tsang, J. Y. & Tse, G. M. Tumor Microenvironment in Breast Cancer—
845 Updates on Therapeutic Implications and Pathologic Assessment. *Cancers* **13**, 4233
846 (2021).
- 847 16. Ge, R., Wang, Z. & Cheng, L. Tumor microenvironment heterogeneity an
848 important mediator of prostate cancer progression and therapeutic resistance. *Npj Precis.*
849 *Oncol.* **6**, 1–8 (2022).
- 850 17. Peng, D. *et al.* Myeloid-Derived Suppressor Cells Endow Stem-like Qualities to
851 Breast Cancer Cells through IL6/STAT3 and NO/NOTCH Cross-talk Signaling. *Cancer*
852 *Res.* **76**, 3156–3165 (2016).
- 853 18. Li, K. *et al.* Myeloid-derived suppressor cells as immunosuppressive regulators
854 and therapeutic targets in cancer. *Signal Transduct. Target. Ther.* **6**, 1–25 (2021).
- 855 19. Lorusso, G. & Ruegg, C. The tumor microenvironment and its contribution to
856 tumor evolution toward metastasis. *Histochem Cell Biol* **130**, 1091–103 (2008).
- 857 20. Sleeman, J. P. *et al.* Concepts of metastasis in flux: the stromal progression
858 model. *Semin Cancer Biol* **22**, 174–86 (2012).
- 859 21. Cha, Y. J. & Koo, J. S. Role of Tumor-Associated Myeloid Cells in Breast Cancer.
860 *Cells* **9**, (2020).
- 861 22. Pastaki Khoshbin, A., Eskian, M., Keshavarz-Fathi, M. & Rezaei, N. Roles of
862 Myeloid-Derived Suppressor Cells in Cancer Metastasis: Immunosuppression and
863 Beyond. *Arch Immunol Ther Exp Warsz* **67**, 89–102 (2019).
- 864 23. Panni, R. Z. *et al.* Tumor-induced STAT3 activation in monocytic myeloid-derived
865 suppressor cells enhances stemness and mesenchymal properties in human pancreatic
866 cancer. *Cancer Immunol. Immunother.* **63**, 513–528 (2014).
- 867 24. Cui, T. X. *et al.* Myeloid-derived suppressor cells enhance stemness of cancer
868 cells by inducing microRNA101 and suppressing the corepressor CtBP2. *Immunity* **39**,

- 869 611–621 (2013).
- 870 25. Abaurrea, A., Araujo, A. M. & Caffarel, M. M. The Role of the IL-6 Cytokine Family
871 in Epithelial–Mesenchymal Plasticity in Cancer Progression. *Int. J. Mol. Sci.* **22**, 8334
872 (2021).
- 873 26. Zarling, J. M. *et al.* Oncostatin M: a growth regulator produced by differentiated
874 histiocytic lymphoma cells. *Proc. Natl. Acad. Sci. U. S. A.* **83**, 9739–9743 (1986).
- 875 27. Felcher, C. M., Bogni, E. S. & Kordon, E. C. IL-6 Cytokine Family: A Putative
876 Target for Breast Cancer Prevention and Treatment. *Int J Mol Sci* **23**, (2022).
- 877 28. Johnson, D. E., O’Keefe, R. A. & Grandis, J. R. Targeting the IL-6/JAK/STAT3
878 signalling axis in cancer. *Nat Rev Clin Oncol* **15**, 234–248 (2018).
- 879 29. Quintas-Cardama, A. & Verstovsek, S. Molecular pathways: Jak/STAT pathway:
880 mutations, inhibitors, and resistance. *Clin Cancer Res* **19**, 1933–40 (2013).
- 881 30. Tawara, K. *et al.* HIGH expression of OSM and IL-6 are associated with
882 decreased breast cancer survival: synergistic induction of IL-6 secretion by OSM and IL-
883 1beta. *Oncotarget* **10**, 2068–2085 (2019).
- 884 31. West, N. R., Murphy, L. C. & Watson, P. H. Oncostatin M suppresses oestrogen
885 receptor- α expression and is associated with poor outcome in human breast cancer.
886 *Endocr. Relat. Cancer* **19**, 181–195 (2012).
- 887 32. Guo, L. *et al.* Stat3-coordinated Lin-28-let-7-HMGA2 and miR-200-ZEB1 circuits
888 initiate and maintain oncostatin M-driven epithelial-mesenchymal transition. *Oncogene*
889 **32**, 5272–5282 (2013).
- 890 33. Araujo, A. M. *et al.* Stromal oncostatin M cytokine promotes breast cancer
891 progression by reprogramming the tumor microenvironment. *J Clin Invest* **132**, (2022).
- 892 34. Bryson, B. L., Junk, D. J., Cipriano, R. & Jackson, M. W. STAT3-mediated SMAD3
893 activation underlies Oncostatin M-induced Senescence. *Cell Cycle* **16**, 319–334 (2017).
- 894 35. Taniguchi, K. & Karin, M. IL-6 and related cytokines as the critical lynchpins
895 between inflammation and cancer. *Semin. Immunol.* **26**, 54–74 (2014).
- 896 36. West, N. R., Murray, J. I. & Watson, P. H. Oncostatin-M promotes phenotypic
897 changes associated with mesenchymal and stem cell-like differentiation in breast cancer.
898 *Oncogene* **33**, 1485–1494 (2014).
- 899 37. Ross, C. *et al.* Metastasis-Specific Gene Expression in Autochthonous and
900 Allograft Mouse Mammary Tumor Models: Stratification and Identification of Targetable
901 Signatures. *Mol. Cancer Res. MCR* **18**, 1278–1289 (2020).
- 902 38. Fico, F., Bousquenaud, M., Rüegg, C. & Santamaria-Martínez, A. Breast Cancer

- 903 Stem Cells with Tumor- versus Metastasis-Initiating Capacities Are Modulated by
904 TGFBR1 Inhibition. *Stem Cell Rep.* **13**, 1–9 (2019).
- 905 39. Hanahan, D. Hallmarks of Cancer: New Dimensions. *Cancer Discov.* **12**, 31–46
906 (2022).
- 907 40. Ouzounova, M. *et al.* Monocytic and granulocytic myeloid derived suppressor cells
908 differentially regulate spatiotemporal tumour plasticity during metastatic cascade. *Nat.*
909 *Commun.* **8**, 14979 (2017).
- 910 41. Veglia, F., Sanseviero, E. & Gabrilovich, D. I. Myeloid-derived suppressor cells in
911 the era of increasing myeloid cell diversity. *Nat. Rev. Immunol.* **21**, 485–498 (2021).
- 912 42. Bronte, V. *et al.* Recommendations for myeloid-derived suppressor cell
913 nomenclature and characterization standards. *Nat. Commun.* **7**, 12150 (2016).
- 914 43. Sebastian, A. *et al.* Single-Cell Transcriptomic Analysis of Tumor-Derived
915 Fibroblasts and Normal Tissue-Resident Fibroblasts Reveals Fibroblast Heterogeneity in
916 Breast Cancer. *Cancers* **12**, 1307 (2020).
- 917 44. Efremova, M., Vento-Tormo, M., Teichmann, S. A. & Vento-Tormo, R.
918 CellPhoneDB: inferring cell–cell communication from combined expression of multi-
919 subunit ligand–receptor complexes. *Nat. Protoc.* **15**, 1484–1506 (2020).
- 920 45. Brandizzi, F. & Barlowe, C. Organization of the ER–Golgi interface for membrane
921 traffic control. *Nat. Rev. Mol. Cell Biol.* **14**, 382–392 (2013).
- 922 46. Chen, K. *et al.* Phenotypically supervised single-cell sequencing parses within-
923 cell-type heterogeneity. *iScience* **24**, 101991 (2021).
- 924 47. Yeo, S. K. *et al.* Single-cell RNA-sequencing reveals distinct patterns of cell state
925 heterogeneity in mouse models of breast cancer. *eLife* **9**, e58810 (2020).
- 926 48. Aouad, P. *et al.* Epithelial-mesenchymal plasticity determines estrogen receptor
927 positive breast cancer dormancy and epithelial reversion drives recurrence. *Nat.*
928 *Commun.* **13**, 4975 (2022).
- 929 49. Jin, W. Role of JAK/STAT3 Signaling in the Regulation of Metastasis, the
930 Transition of Cancer Stem Cells, and Chemoresistance of Cancer by Epithelial–
931 Mesenchymal Transition. *Cells* **9**, 217 (2020).
- 932 50. Junk, D. J. *et al.* Oncostatin M promotes cancer cell plasticity through cooperative
933 STAT3-SMAD3 signaling. *Oncogene* **36**, 4001–4013 (2017).
- 934 51. Naz, F., Shi, M., Sajid, S., Yang, Z. & Yu, C. Cancer stem cells: a major culprit of
935 intra-tumor heterogeneity. *Am. J. Cancer Res.* **11**, 5782–5811 (2021).
- 936 52. Zhang, R., Tu, J. & Liu, S. Novel molecular regulators of breast cancer stem cell

- 937 plasticity and heterogeneity. *Semin Cancer Biol* **82**, 11–25 (2022).
- 938 53. Qin, S. *et al.* Emerging role of tumor cell plasticity in modifying therapeutic
939 response. *Signal Transduct. Target. Ther.* **5**, 228 (2020).
- 940 54. Kong, D., Hughes, C. J. & Ford, H. L. Cellular Plasticity in Breast Cancer
941 Progression and Therapy. *Front. Mol. Biosci.* **7**, 72 (2020).
- 942 55. Muzio, G., Maggiora, M., Paiuzzi, E., Oraldi, M. & Canuto, R. A. Aldehyde
943 dehydrogenases and cell proliferation. *Free Radic. Biol. Med.* **52**, 735–746 (2012).
- 944 56. Curtis, C. *et al.* The genomic and transcriptomic architecture of 2,000 breast
945 tumours reveals novel subgroups. *Nature* **486**, 346–352 (2012).
- 946 57. Shen, M. *et al.* A review of current progress in triple-negative breast cancer
947 therapy. *Open Med Wars* **15**, 1143–1149 (2020).
- 948 58. Al-Mahmood, S., Sapiezynski, J., Garbuzenko, O. B. & Minko, T. Metastatic and
949 triple-negative breast cancer: challenges and treatment options. *Drug Deliv Transl Res* **8**,
950 1483–1507 (2018).
- 951 59. Azim, H. A., Ghosn, M., Oualla, K. & Kassem, L. Personalized treatment in
952 metastatic triple-negative breast cancer: The outlook in 2020. *Breast J* **26**, 69–80 (2020).
- 953 60. Vagia, E., Mahalingam, D. & Cristofanilli, M. The Landscape of Targeted
954 Therapies in TNBC. *Cancers Basel* **12**, (2020).
- 955 61. Hua, Z., White, J. & Zhou, J. Cancer stem cells in TNBC. *Semin Cancer Biol* **82**,
956 26–34 (2022).
- 957 62. Battle, E. & Clevers, H. Cancer stem cells revisited. *Nat Med* **23**, 1124–1134
958 (2017).
- 959 63. Brooks, M. D., Burness, M. L. & Wicha, M. S. Therapeutic Implications of Cellular
960 Heterogeneity and Plasticity in Breast Cancer. *Cell Stem Cell* **17**, 260–71 (2015).
- 961 64. Yeo, S. K., Wen, J., Chen, S. & Guan, J. L. Autophagy Differentially Regulates
962 Distinct Breast Cancer Stem-like Cells in Murine Models via EGFR/Stat3 and
963 Tgfbeta/Smad Signaling. *Cancer Res* **76**, 3397–410 (2016).
- 964 65. Gong, J. *et al.* Genotoxic stress induces Sca-1-expressing metastatic mammary
965 cancer cells. *Mol. Oncol.* **12**, 1249–1263 (2018).
- 966 66. Shimokawa, M. *et al.* Visualization and targeting of LGR5+ human colon cancer
967 stem cells. *Nature* **545**, 187–192 (2017).
- 968 67. Oo, M. W. *et al.* Resident stroma-secreted chemokine CCL2 governs myeloid-
969 derived suppressor cells in the tumor microenvironment. *JCI Insight* **7**, (2022).
- 970 68. Franklin, D. A. *et al.* MEK activation modulates glycolysis and supports

- 971 suppressive myeloid cells in TNBC. *JCI Insight* **5**, (2020).
- 972 69. Bullock, K. & Richmond, A. Suppressing MDSC Recruitment to the Tumor
973 Microenvironment by Antagonizing CXCR2 to Enhance the Efficacy of Immunotherapy.
974 *Cancers Basel* **13**, (2021).
- 975 70. Jovanovic, I. P. *et al.* Interleukin-33/ST2 axis promotes breast cancer growth and
976 metastases by facilitating intratumoral accumulation of immunosuppressive and innate
977 lymphoid cells. *Int J Cancer* **134**, 1669–82 (2014).
- 978 71. Szczerba, B. M. *et al.* Neutrophils escort circulating tumour cells to enable cell
979 cycle progression. *Nature* **566**, 553–557 (2019).
- 980 72. Doherty, M. R. *et al.* The opposing effects of interferon-beta and oncostatin-M as
981 regulators of cancer stem cell plasticity in triple-negative breast cancer. *Breast Cancer*
982 *Res* **21**, 54 (2019).
- 983 73. Cavalli, L. R., Riggins, R. B., Wang, A., Clarke, R. & Haddad, B. R. Frequent loss
984 of heterozygosity at the interferon regulatory factor-1 gene locus in breast cancer. *Breast*
985 *Cancer Res. Treat.* **121**, 227–231 (2010).
- 986 74. Weichselbaum, R. R. *et al.* An interferon-related gene signature for DNA damage
987 resistance is a predictive marker for chemotherapy and radiation for breast cancer. *Proc.*
988 *Natl. Acad. Sci. U. S. A.* **105**, 18490–18495 (2008).
- 989 75. Aljohani, A. I. *et al.* Myxovirus resistance 1 (MX1) is an independent predictor of
990 poor outcome in invasive breast cancer. *Breast Cancer Res. Treat.* **181**, 541–551 (2020).
- 991 76. Chan, J. M. *et al.* Lineage plasticity in prostate cancer depends on JAK/STAT
992 inflammatory signaling. *Science* **377**, 1180–1191 (2022).
- 993 77. Deng, S. *et al.* Ectopic JAK–STAT activation enables the transition to a stem-like
994 and multilineage state conferring AR-targeted therapy resistance. *Nat. Cancer* **3**, 1071–
995 1087 (2022).
- 996 78. Lynce, F. *et al.* Phase I study of JAK1/2 inhibitor ruxolitinib with weekly paclitaxel
997 for the treatment of HER2-negative metastatic breast cancer. *Cancer Chemother*
998 *Pharmacol* **87**, 673–679 (2021).
- 999 79. Kearney, M. *et al.* Phase I/II trial of ruxolitinib in combination with trastuzumab in
1000 metastatic HER2 positive breast cancer. *Breast Cancer Res Treat* **189**, 177–185 (2021).
- 1001 80. O’Shaughnessy, J. *et al.* A randomized, double-blind, phase 2 study of ruxolitinib
1002 or placebo in combination with capecitabine in patients with advanced HER2-negative
1003 breast cancer and elevated C-reactive protein, a marker of systemic inflammation. *Breast*
1004 *Cancer Res Treat* **170**, 547–557 (2018).

- 1005 81. Lan, Q. *et al.* Type I interferon/IRF7 axis instigates chemotherapy-induced
1006 immunological dormancy in breast cancer. *Oncogene* **38**, 2814–2829 (2019).
- 1007 82. FASTQC. A quality control tool for high throughput sequence data | BibSonomy.
1008 <https://www.bibsonomy.org/bibtex/f230a919c34360709aa298734d63dca3>.
- 1009 83. Ewels, P., Magnusson, M., Lundin, S. & Källér, M. MultiQC: summarize analysis
1010 results for multiple tools and samples in a single report. *Bioinformatics* **32**, 3047–3048
1011 (2016).
- 1012 84. Bolger, A. M., Lohse, M. & Usadel, B. Trimmomatic: a flexible trimmer for Illumina
1013 sequence data. *Bioinformatics* **30**, 2114–2120 (2014).
- 1014 85. Kopylova, E., Noé, L. & Touzet, H. SortMeRNA: fast and accurate filtering of
1015 ribosomal RNAs in metatranscriptomic data. *Bioinforma. Oxf. Engl.* **28**, 3211–3217
1016 (2012).
- 1017 86. Anders, S., Pyl, P. T. & Huber, W. HTSeq—a Python framework to work with high-
1018 throughput sequencing data. *Bioinformatics* **31**, 166–169 (2015).
- 1019 87. Patro, R., Duggal, G., Love, M. I., Irizarry, R. A. & Kingsford, C. Salmon provides
1020 fast and bias-aware quantification of transcript expression. *Nat. Methods* **14**, 417–419
1021 (2017).
- 1022 88. <https://www.r-project.org/>.
- 1023 89. Love, M. I., Huber, W. & Anders, S. Moderated estimation of fold change and
1024 dispersion for RNA-seq data with DESeq2. *Genome Biol.* **15**, 550 (2014).
- 1025 90. Hänzelmann, S., Castelo, R. & Guinney, J. GSEA: gene set variation analysis for
1026 microarray and RNA-Seq data. *BMC Bioinformatics* **14**, 7 (2013).
- 1027 91. Morgan M, Falcon S, Gentleman R. GSEABase: Gene set enrichment data
1028 structures and methods. R package version 1.58.0. (2022).
- 1029 92. Subramanian, A. *et al.* Gene set enrichment analysis: A knowledge-based
1030 approach for interpreting genome-wide expression profiles. *Proc. Natl. Acad. Sci.* **102**,
1031 15545–15550 (2005).
- 1032 93. Ritchie, M. E. *et al.* limma powers differential expression analyses for RNA-
1033 sequencing and microarray studies. *Nucleic Acids Res.* **43**, e47 (2015).
- 1034 94. Kolde, R. Pheatmap: pretty heatmaps. *R Package Version* **1**, 726 (2012).
- 1035 95. Dusa, Adrian. Draw Venn Diagrams R package venn. (2016).
- 1036 96. Wickham, H. *et al.* Welcome to the Tidyverse. *J. Open Source Softw.* **4**, 1686
1037 (2019).
- 1038 97. Wickham, H. *ggplot2*. (Springer, 2009). doi:10.1007/978-0-387-98141-3.

- 1039 98. Gu, Z., Gu, L., Eils, R., Schlesner, M. & Brors, B. circlize Implements and
1040 enhances circular visualization in R. *Bioinforma. Oxf. Engl.* **30**, 2811–2812 (2014).
- 1041 99. Durinck, S. *et al.* BioMart and Bioconductor: a powerful link between biological
1042 databases and microarray data analysis. *Bioinforma. Oxf. Engl.* **21**, 3439–3440 (2005).
- 1043 100. Durinck, S., Spellman, P. T., Birney, E. & Huber, W. Mapping identifiers for the
1044 integration of genomic datasets with the R/Bioconductor package biomaRt. *Nat. Protoc.*
1045 **4**, 1184–1191 (2009).
- 1046 101. Neuwirth, E. RColorBrewer: ColorBrewer Palettes. 5.
- 1047 102. Wu, T. *et al.* clusterProfiler 4.0: A universal enrichment tool for interpreting omics
1048 data. *Innov. Camb. Mass* **2**, 100141 (2021).
- 1049 103. Yu, G., Wang, L.-G., Han, Y. & He, Q.-Y. clusterProfiler: an R package for
1050 comparing biological themes among gene clusters. *Omics J. Integr. Biol.* **16**, 284–287
1051 (2012).
- 1052 104. Yu, G. & Hu, E. enrichplot: Visualization of Functional Enrichment Result. (2022)
1053 doi:10.18129/B9.bioc.enrichplot.
- 1054 105. Xu, S. *et al.* Use ggbreak to Effectively Utilize Plotting Space to Deal With Large
1055 Datasets and Outliers. *Front. Genet.* **12**, 774846 (2021).
- 1056 106. Monnier, Y. *et al.* CYR61 and alphaVbeta5 integrin cooperate to promote invasion
1057 and metastasis of tumors growing in preirradiated stroma. *Cancer Res.* **68**, 7323–7331
1058 (2008).
- 1059 107. Kassambara, A. ggpubr: ‘ggplot2’ Based Publication Ready Plots. (2020).
- 1060 108. Stuart, T. *et al.* Comprehensive Integration of Single-Cell Data. *Cell* **177**, 1888-
1061 1902.e21 (2019).
- 1062 109. Gu, Z., Eils, R. & Schlesner, M. Complex heatmaps reveal patterns and
1063 correlations in multidimensional genomic data. *Bioinforma. Oxf. Engl.* **32**, 2847–2849
1064 (2016).
- 1065 110. Shao, X. *et al.* CellTalkDB: a manually curated database of ligand–receptor
1066 interactions in humans and mice. *Brief. Bioinform.* **22**, bbaa269 (2021).
- 1067 111. Cabello-Aguilar, S. *et al.* SingleCellSignalR: inference of intercellular networks
1068 from single-cell transcriptomics. *Nucleic Acids Res.* **48**, e55 (2020).
- 1069 112. Trapnell, C. *et al.* The dynamics and regulators of cell fate decisions are revealed
1070 by pseudotemporal ordering of single cells. *Nat. Biotechnol.* **32**, 381–386 (2014).
- 1071 113. Qiu, X. *et al.* Reversed graph embedding resolves complex single-cell trajectories.
1072 *Nat. Methods* **14**, 979–982 (2017).

- 1073 114. Cao, J. *et al.* The single-cell transcriptional landscape of mammalian
1074 organogenesis. *Nature* **566**, 496–502 (2019).
- 1075 115. McInnes, L., Healy, J. & Melville, J. UMAP: Uniform Manifold Approximation and
1076 Projection for Dimension Reduction. Preprint at <http://arxiv.org/abs/1802.03426> (2020).
- 1077 116. Korotkevich, G. *et al.* Fast gene set enrichment analysis. 060012 Preprint at
1078 <https://doi.org/10.1101/060012> (2021).
- 1079 117. Gao, W. *et al.* IL20RA signaling enhances stemness and promotes the formation
1080 of an immunosuppressive microenvironment in breast cancer. *Theranostics* **11**, 2564–
1081 2580 (2021).
- 1082 118. Cerami, E. *et al.* The cBio cancer genomics portal: an open platform for exploring
1083 multidimensional cancer genomics data. *Cancer Discov.* **2**, 401–404 (2012).
- 1084 119. Ramos, M. *et al.* Multiomic Integration of Public Oncology Databases in
1085 Bioconductor. *JCO Clin. Cancer Inform.* 958–971 (2020) doi:10.1200/CCI.19.00119.
- 1086 120. Therneau, T. M. & Grambsch, P. M. *Modeling Survival Data: Extending the Cox*
1087 *Model.* (Springer, 2000). doi:10.1007/978-1-4757-3294-8.

1088

1089 **Acknowledgments**

1090 The authors wish to thank Sarah Cattin and Melissa Rizzo for assistance with FACS
1091 analysis, Dr. Ana-Marija Sulić (Institute of Biotechnology, HiLIFE, University of Helsinki) for
1092 the insightful discussion about scRNA-seq data analysis, Dr. Fred R. Miller (Michigan
1093 Cancer Foundation, Detroit, MI, USA) for providing 4T1 cells, Dr. Khalil Zaman (Department
1094 of Oncology, University Hospital, University of Lausanne, Lausanne, Switzerland) for
1095 providing chemotherapeutic drugs. This work was supported by grants from the Swiss
1096 National Science Foundation (31003A_179248; 310030_208136), the Swiss Cancer
1097 League (KFS 4400-02-2018) and the Medic Foundation (to C.R.).

1098

1099 **Author contributions**

1100 Conceptualization, S.P., Q.L., C.R.; Methodology, S.P., N.F., Q.L., C.R.; Software,
1101 A.K., N.F., Q.L.; Validation, S.P., M.B., A.K., Q.L.; Formal analysis, S.P., M.B., A.K., Q.L.;

1102 Investigation, S.P., M.B., A.K., O.C., Y-T.H., N.D., L.G., Q.L.; Resources, S.P., M.B., A.K.,
1103 O.C., N.D., L.G., G.L.; Data Curation, S.P., M.B., A.K., N.D., Q.L., C.R.; Writing – original
1104 draft preparation, S.P., Q.L., C.R.; Writing – review and editing, S.P., M.B., A.K., Y-T.H.,
1105 G.L., N.D., Q.L., C.R.; Visualization, S.P., M.B., A.K., Q.L., C.R.; Supervision, S.P., Q.L.,
1106 C.R.; Project administration, Q.L., C.R.; Funding acquisition, C.R.

1107

1108 **Competing interests**

1109 The authors have no conflicts of interest to declare.

Sca1 (Ross dataset)

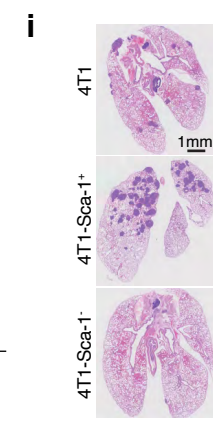
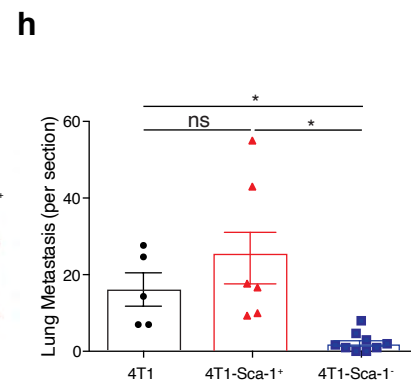
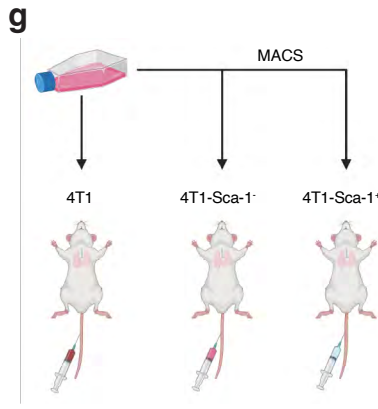
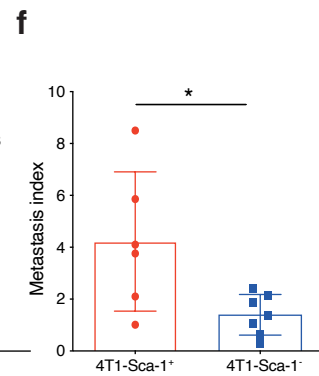
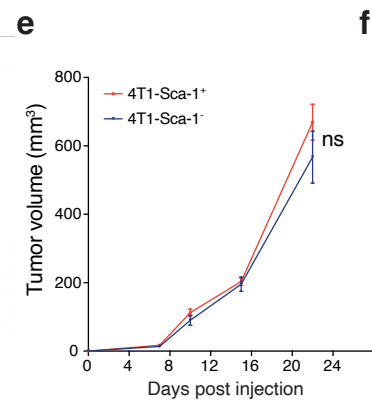
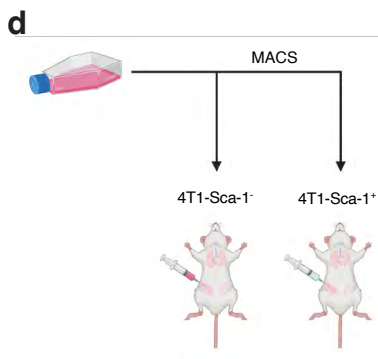
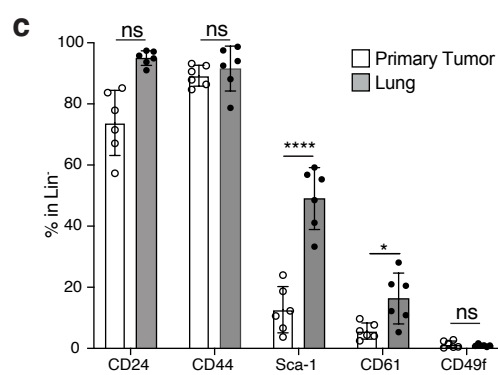
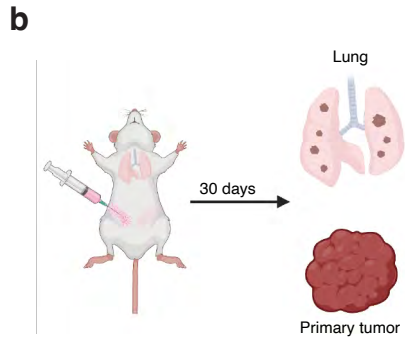
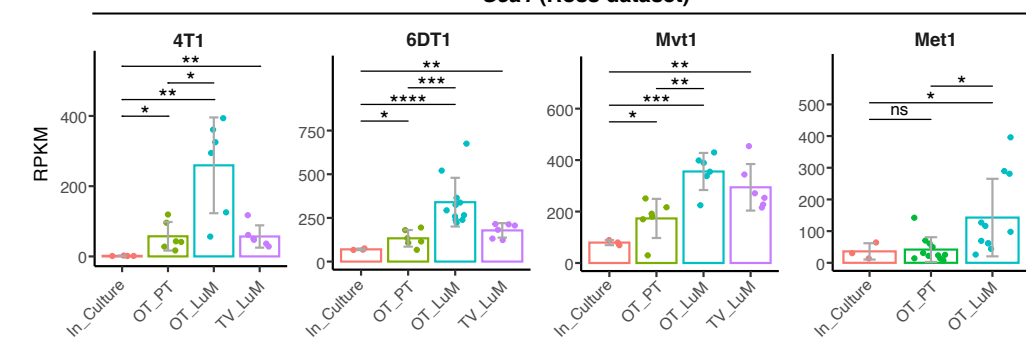


Figure 1

Figure 1. Sca-1⁺ population is enriched during *in vivo* metastasis across multiple breast cancer models

(a) Sca-1 mRNA expression in the metastatic murine breast cancer models 4T1, 6DT1, Mvt1 and Met1, extracted from the Ross dataset. Analyzed samples consist of cultured cells (In_Culture), orthotopic injected primary tumors (OP_PT), spontaneous lung metastases (OP_LuM) and lung metastases induced by tail-vein injection (TV_LuM). Data are presented as mean of Reads Per Kilobase of transcript per Million mapped reads (RPKM) \pm SD (unpaired two-tailed student's t test with Bonferroni correction).

(b) Experimental set up for *in vivo* experimental validation. The 4T1 tumor cells were orthotopically injected into the 4th mammary fat pad. Thirty days later, cells from primary tumors and lungs were isolated to examine CSC marker expression by flow cytometry.

(c) Frequency of CSC marker expression in primary tumors and lung metastases. Results give the percentage of CD24, CD44, Sca-1, CD61 and CD49f positive cells gated in lineage negative cells (CD45⁻CD31⁻TER119⁻).

(d-f) Experimental set up **(d)** of the *in vivo* experiment to assess tumor growth **(e)** and lung metastatic ability (metastatic index) **(f)** of 4T1-Sca-1⁺ and 4T1-Sca-1⁻ populations isolated from parental 4T1 cells orthotopically injected into the 4th mammary fat pad. Metastases are assessed 21 days after tumor cell injection. n=8/group, 3 independent experiments.

(g-i) Experimental set up **(g)** of the *in vivo* experiment to assess lung colonization capacity of sorted parental 4T1, 4T1-Sca-1⁺ and 4T1-Sca-1⁻ cells by tail-vein injection. Lung metastatic nodule numbers **(h)** and representative images **(i)** of lungs from mice 10 days post injection (n=5-6, 2 independent experiments). Scale bar=1 mm. Data are

represented as mean values \pm SEM (unpaired two-tailed student's t test). P values: *, $p < 0.05$; **, $p < 0.01$; ***, $p < 0.001$; ****, $p < 0.0001$; ns, non-significant.

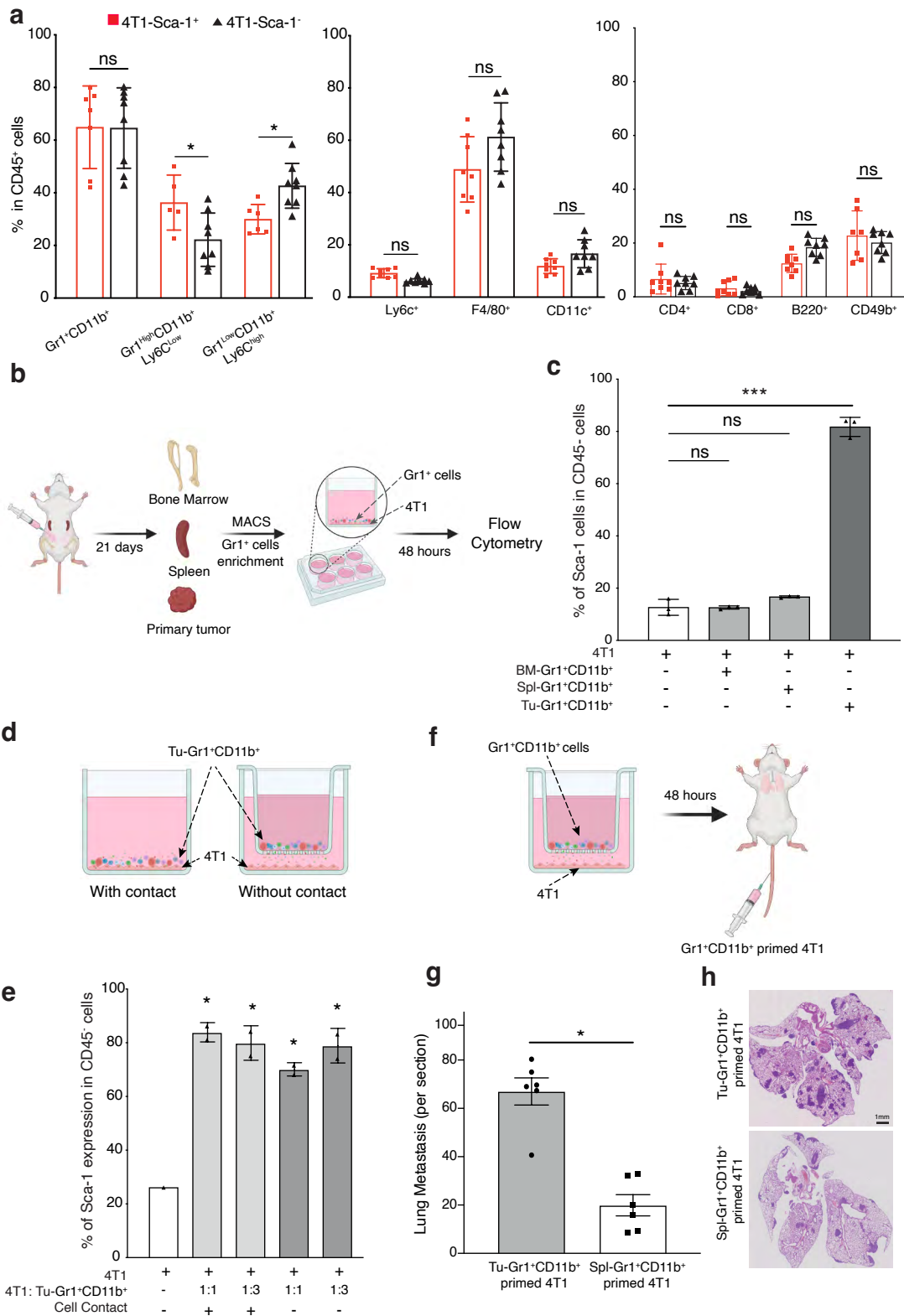


Figure 2

Figure 2. Sca-1 expression is modulated by the tumor microenvironment

(a) Frequency of different immune cell populations in primary tumors of mice orthotopically injected with 4T1-Sca-1⁺ and 4T1-Sca-1⁻ 21 days post injection. Populations are determined in CD45 negative, viable cells.

(b-c) Illustrative scheme **(b)** showing the experimental design for isolating Gr1⁺ cells from different sites of tumor-bearing mice. Twenty-one days after tumor implantation, Gr1⁺ cells were isolated from bone marrow (BM-Gr1⁺CD11b⁺), spleen (Spl-Gr1⁺CD11b⁺) or primary tumor (Tu-Gr1⁺CD11b⁺) and co-cultured for 48 hours with parental 4T1 cells *in vitro*. Sca-1 expression in tumor cells was examined by flow cytometry **(c)**. Co-cultures conditions are indicated in the bar graph.

(d) Illustrative scheme of the experimental co-culture setup.

(e) MACS-enriched Gr1⁺ cells were cocultured with 4T1 cells with or without Transwell inserts of 0.4 μ m pore size. The 4T1 cells were seeded in the bottom well and Gr1⁺CD11b⁺ cells in the upper part of the insert. After 48 hours, 4T1 cells were examined for Sca1 expression by FACS. Co-cultures conditions are indicated in the bar graph. The ratio of tumor cells and Tu-Gr1⁺CD11b⁺ is varied from 1:1 to 1:3. Significant enrichment of Sca-1⁺ population were observed in all conditions.

(f) Illustrative scheme of the experimental metastasis setup.

(g-h) Evaluation of the metastatic capacity of Gr1⁺CD11b⁺-educated 4T1 cells *in vivo*. The 4T1 tumor cells were primed with Tu-Gr1⁺CD11b⁺ or Spl-Gr1⁺CD11b⁺ *in vitro* without cell-cell contact for 48 hours and injected into the tail vein of mice. Lung metastases were quantified 10 days after injection **(g)**, and representative images of lung sections are showed **(h)**. n=7, H&E staining, Scale bar=1mm.

Data are represented as mean values \pm SEM. P values: *, p<0.05; ***, p< 0.001 (unpaired two-tailed student's t test, and only significant data has been labeled).

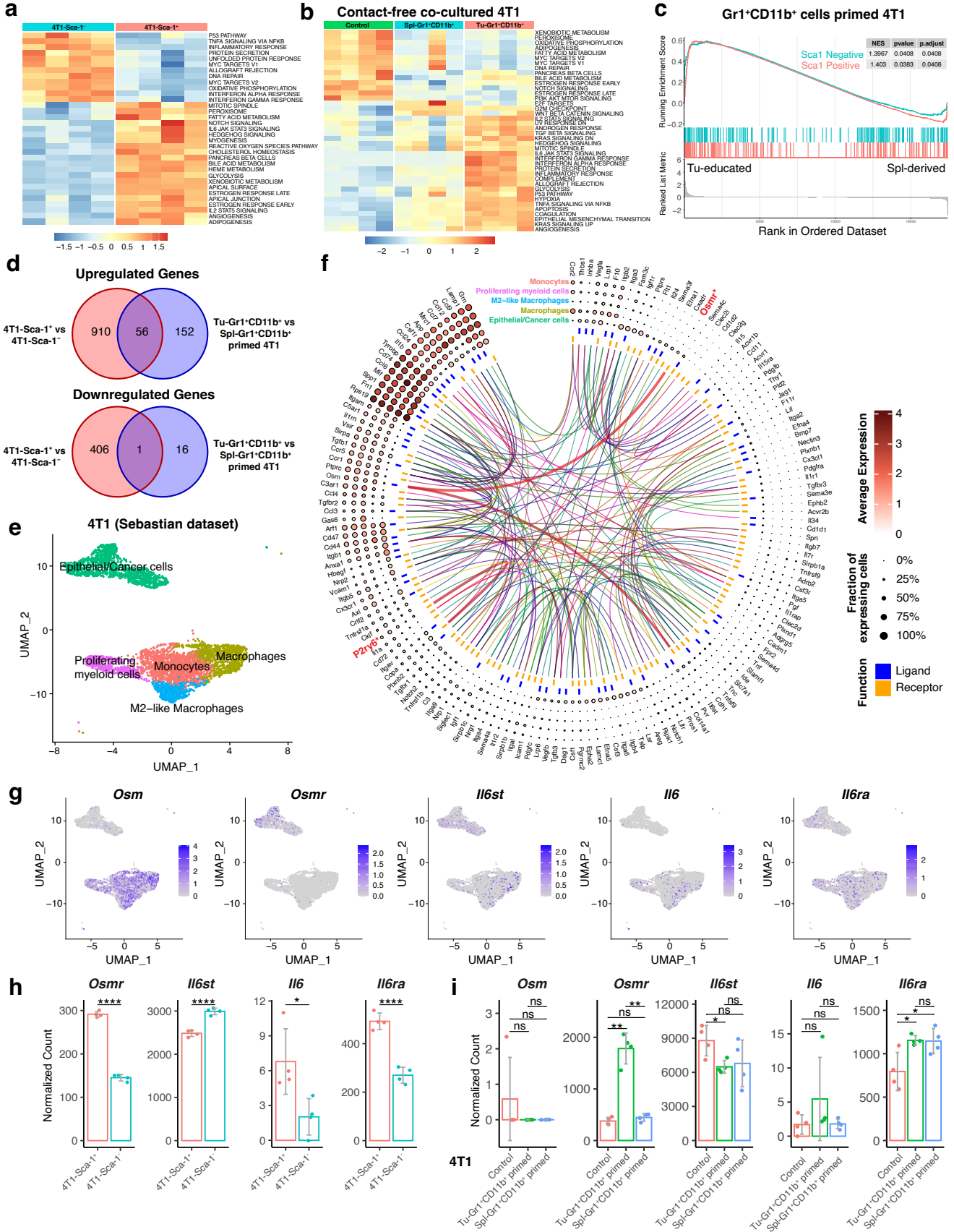


Figure 3

Figure 3. Transcriptomic analysis of Sca-1⁺ tumor cells

(a) Heatmap showing the signature score of the hallmark pathways analysis in 4T1-Sca-1⁺ and 4T1-Sca-1⁻ population sorted from parental 4T1 cells. The colors code the expression levels relative to average levels as indicate at the bottom.

(b) Heatmap showing the signature score of the hallmarks pathway analysis in parental 4T1 (4T1), Spl-Gr1⁺CD11b⁺ primed 4T1 and Tu-Gr1⁺CD11b⁺ primed 4T1 cells. The colors code the expression levels relative to average levels as indicate at the bottom.

(c) Gene set enrichment analysis (GSEA) comparing the Tu-Gr1⁺CD11b⁺ and Spl-Gr1⁺CD11b⁺ primed 4T1 cells. GSEA shows positive correlations of both Sca1 Positive and Sca1 Negative signatures. NES, normalized enrichment score.

(d) Venn diagrams showing that 56 upregulated genes, and 1 downregulated gene are shared between endogenous and Tu-Gr1⁺CD11b⁺ induced Sca-1⁺ population in 4T1 tumor cells.

(e) UMAP plot showing clusters of cancer cells and myeloid cell populations in orthotopically growing 4T1-derived primary tumors extracted from the Sebastian dataset (see Materials and Methods for details)-

(f) Circos diagram showing the potential interactions between cancer cells and different myeloid cell populations determined by CellPhoneDB (see Materials and Methods for details) based on the Sebastian dataset. Only OSMR and P2RY6 are shared with the common 56 gene list showed in panel **d**.

(g) UMAP plot showing the gene expression pattern of *Osm*, *Osmr*, *Il6st*, *Il6* and *Il6ra* in different cell populations in the Sebastian dataset.

(h-i) mRNA expression of *Osm*, *Osmr*, *Il6st*, *Il6* and *Il6ra* based on RNAseq data used to generate the heatmaps shown in **a** & **b**, respectively. *Osm* expression is not detected in sorted 4T1 cells. Data are presented as mean of normalized count \pm SD. P values:

, $p < 0.05$; **, $p < 0.01$; ***, $p < 0.001$; ****, $p < 0.0001$; ns, non-significant (unpaired two-tailed student's t test, and with Bonferroni correction for Gr1⁺CD11b⁺ cells-educated 4T1 cells).

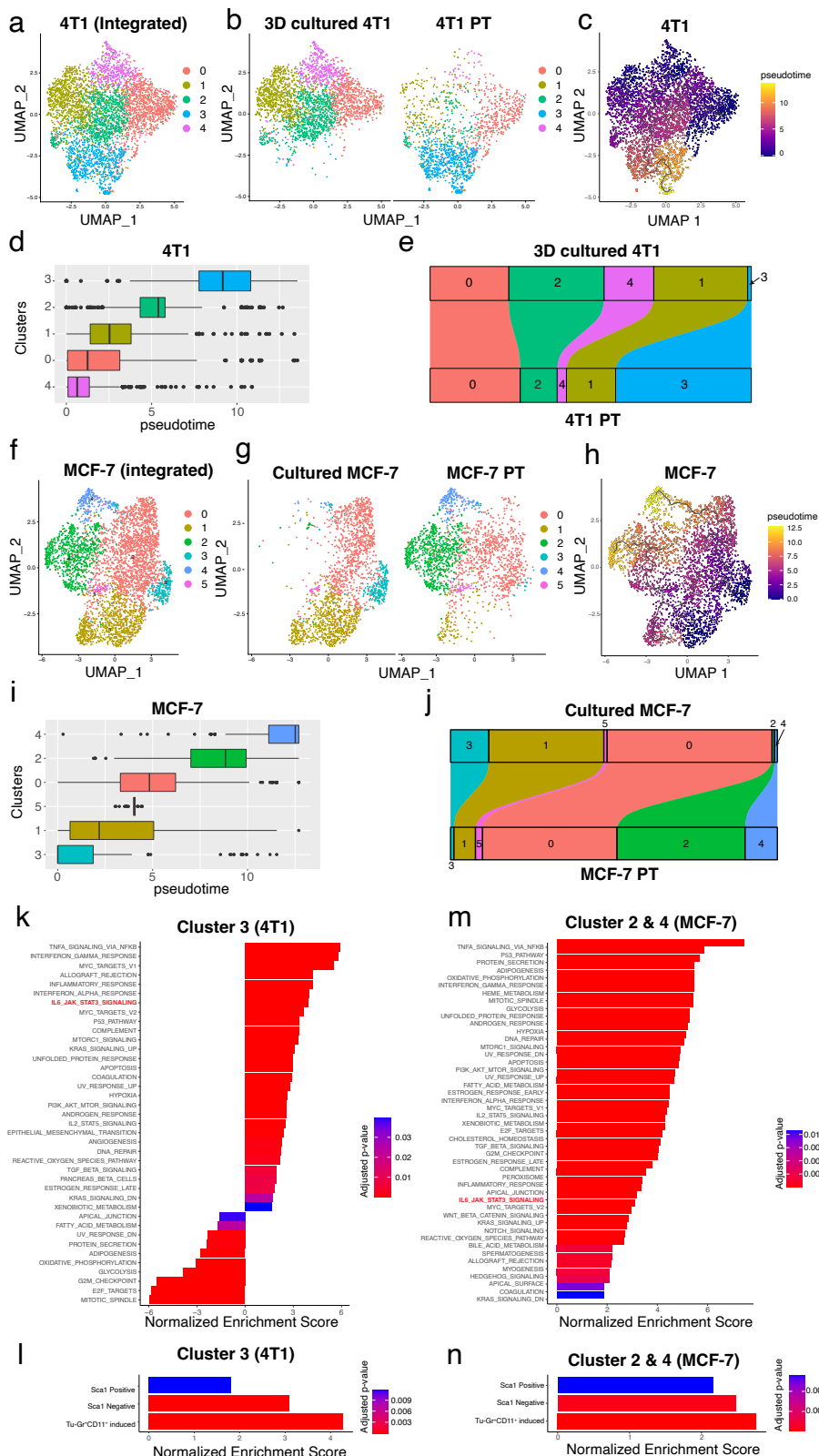


Figure 4

Figure 4. Transformation dynamics of tumor cell populations induced by the tumor microenvironment

(a) UMAP plots showing 4T1 clusters based on integrated scRNA-seq data from 4T1 cells in 3D culture or in primary tumor.

(b) Distribution of specific clusters in 4T1 cells in 3D culture or in primary tumor (PT).

(c-d) UMAP plot **(c)** and boxplot **(d)** showing the clusters in pseudo-time during the transformation of 4T1 cells from *ex vivo* culture to *in vivo*.

(e) Sankey diagram showing the dynamic of each cluster during the transformation of 4T1 cells from *ex vivo* culture to *in vivo*. Cluster 3 was largely expanded *in vivo*.

(f) UMAP plots showing MCF-7 clusters based on integrated scRNA-seq data from MCF-7 cells in culture or in primary tumor.

(g) Distribution of the specific clusters in cultured MCF7 cells or in MCF7 primary tumors (PT).

(h-i) UMAP plot **(h)** and boxplot **(i)** showing the clusters in pseudo-time during the transformation of MCF-7 cells from *ex vivo* culture to *in vivo*.

(e) Sankey diagram showing the dynamic of each cluster during the transformation of MCF-7 cells from *ex vivo* culture to *in vivo*. Cluster 2 and 4 were largely expanded *in vivo*.

(k-l) GESA analysis of Hallmark gene sets **(k)** and Sca1 Positive signature, Sca1 Negative Signature and Tu-Gr1⁺CD11b⁺ induced signature **(l)** of cluster 3 in 4T1 data. Only the signatures with adjusted p-value <0.05 were shown.

(m-n) GESA analysis of Hallmark gene sets **(m)** and Sca1 Positive signature, Sca1 Negative Signature and Tu-Gr1⁺CD11b⁺ induced signature **(n)** of cells in cluster 2 or cluster 4 in MCF-7 data. Only the signatures with adjusted p-value <0.05 were shown.

Analyses are based on publicly available data (4T1: GSM4812003 and GSM3502134;
MCF-7: GSM4681765 and GSM5904917).

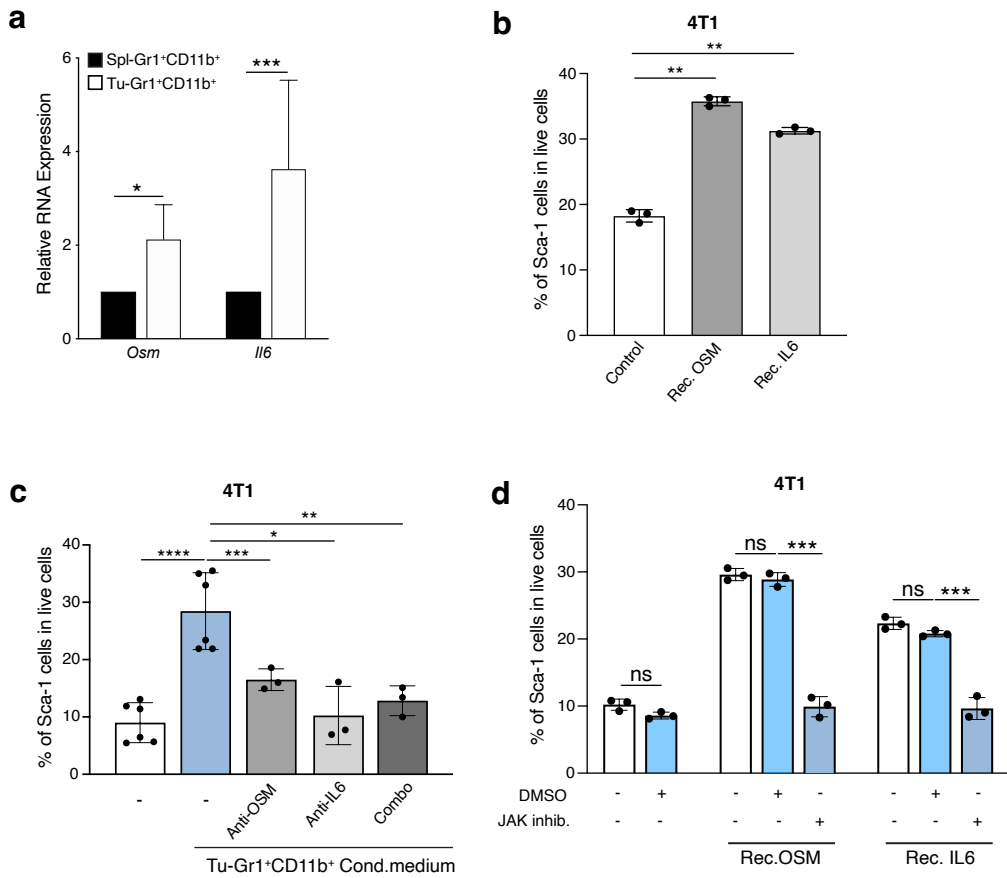


Figure 5

Figure 5. Sca-1⁺ population is modulated by the OSM/IL6-JAK pathway

(a) Quantitative PCR analysis of *Osm* and *Il6* mRNA expression in Tu-Gr1⁺CD11b⁺ and Spl- Gr1⁺CD11b⁺. Tu-Gr1⁺CD11b⁺ express significantly higher *Osm* and *Il6* levels compared with Spl-Gr1⁺CD11b⁺.

(b) Fraction of 4T1-Sca1⁺ cells upon exposure to recombinant Il6 or Osm protein (1 µg/ml for 48 hours) as determined by flow cytometry. Both cytokines induced the Sca-1⁺ population in cultured 4T1 tumor cells.

(c) Inhibition of OSM and IL6 from Tu-Gr1⁺CD11b⁺ conditioned medium with anti- OSM or anti-IL6 neutralizing antibody as indicated. Treatment with either antibody significantly suppressed the Sca-1⁺ population enrichment.

(d) Treatment with the JAK inhibitor Ruxolitinib (5 µM) of cultured 4T1 cells stimulated with recombinant IL6 or OSM protein (1 µg/ml, 48 hours exposure) as indicated. Ruxolitinib inhibited Sca-1⁺ population enrichment induced by recombinant IL6 or OSM protein.

Data are represented as mean ± SEM. *, p<0.05; **, p< 0.01; ***, p< 0.001; ****, p< 0.0001; ns, non-significant (unpaired two-tailed student's t test, and only significant data has been labeled).

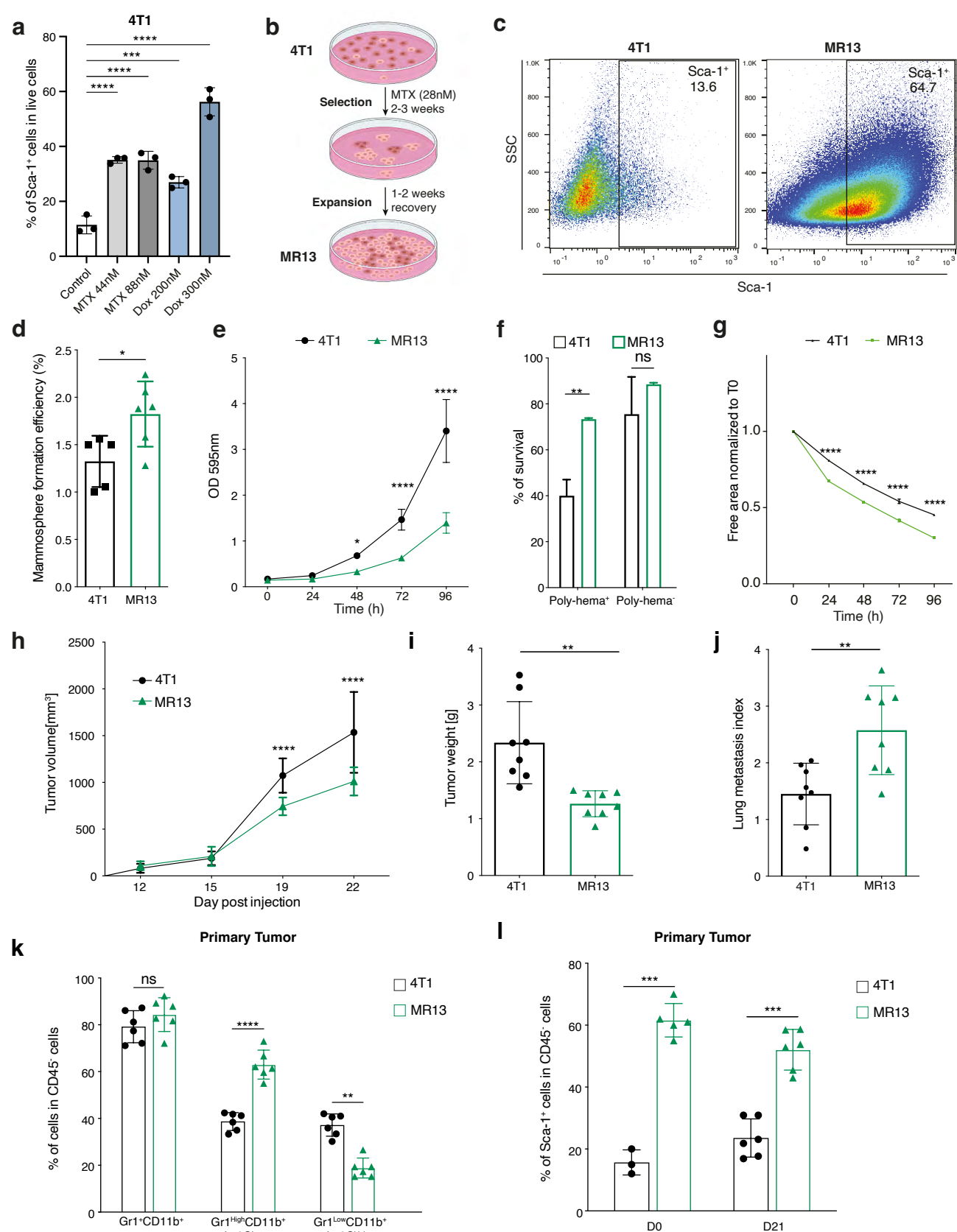


Figure 6

Figure 6. Long term chemotherapy treatment of 4T1 cells induces a stable Sca-1⁺ population (MR13) with higher metastatic capacity and CSC features

(a) Fraction of 4T1-Sca1⁺ cells upon short-term (48 hours) Methotrexate (44 and 88 nM) and Doxorubicin (200 and 300 nM) treatments. All treatments induced enrichment of Sca-1⁺ population.

(b) Illustrative scheme of the experimental design to obtain chemotherapy resistant MR13 cells from 4T1.

(c) Dot plots representing Sca-1 expression vs SSC determined by flow cytometry in MR13 chemotherapy resistant cells vs parental 4T1 tumor cells *in vitro*.

(d) Quantification of the mammosphere forming efficiency of 4T1 and MR13 tumor cells.

(e) Cell proliferation curve of 4T1 and MR13 tumor cells *in vitro* determined by crystal violet assay. The results are presented as mean of optical density (OD).

(f) Anchorage free survival of 4T1 and MR13 tumor cells given in % of surviving cells.

(g) Cell motility of 4T1 and MR13 tumor cells determined by a scratch wound healing assay. n=5-6/group. Results are presented as cell-free area relative to the initial wound area from 3 independent experiments.

(h) Growth curves of primary tumors in BALB/c mice orthotopically injected with 4T1 and MR13 tumor cells (n=10-11/group).

(i) Tumor weight of 4T1 and MR13 tumors recovered from BALB/c mice at day 22 post injection (n=8-9/group).

(j) Lung metastasis index 23 days post injection. The number of metastatic nodules is determined by H&E staining and normalized based on the primary tumor weight (n=8-9/group).

(k) Frequency of different CD11b⁺ myeloid cells subpopulations in primary tumors from MR13 and 4T1 injected mice determined by flow cytometry 21-days post injection (n=6). Subpopulations are determined in CD45 positive, viable cell population.

(l) Percentage of Sca-1⁺ tumor cells at time of injections (D0) of 4T1 and MR13 cells and in primary tumors recovered at day 21 (D21). Sca-1 expression is determined in CD45 negative, viable cell population.

Data are represented as mean values \pm SEM. *, p<0.05; **, p<0.005; ***, p< 0.001, ****, p< 0.0001 unpaired two-tailed student's t test, and only significant data has been labeled. In e, g, h, results were analyzed by two-way ANOVA with Tukey's multiple comparison test.

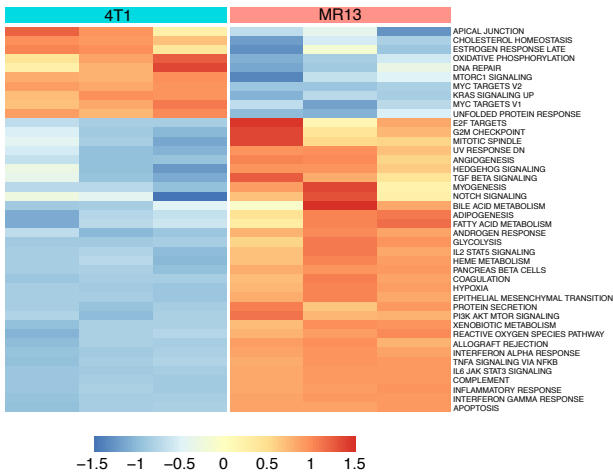
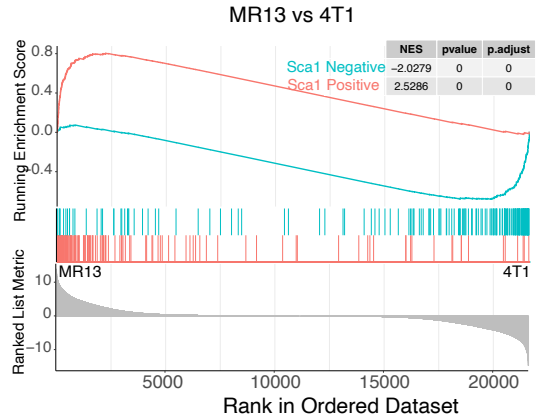
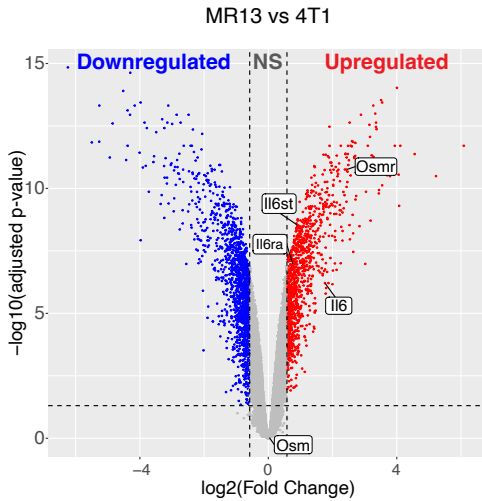
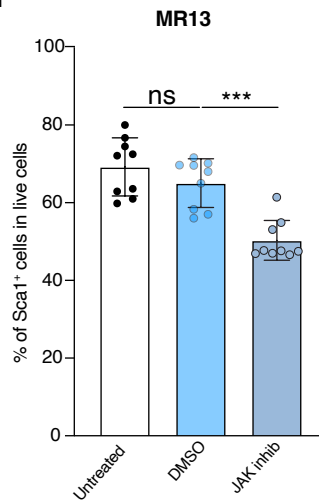
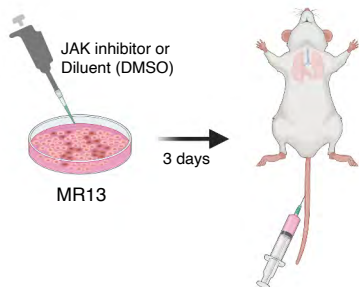
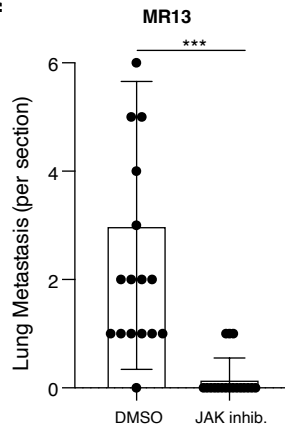
a**b****c****d****e****f**

Figure 7

Figure 7. IL6-JAK pathway promotes Sca-1⁺ persistence and metastatic capacity in chemotherapy resistant MR13 tumor cells

(a-b) Gene expression analysis of parental 4T1 and chemotherapy resistant MR13 cells. Heat map represents the signature score of the hallmark pathways analysis. Results from 3 biological replicates are shown **(a)**. GSEA results showing that MR13 cells are positively enriched with for the Sca-1 Positive signature and negatively with for the Sca-1 Negative signature **(b)**.

(c) Volcano plot showing the differential expression of *Osm*, *Osmr*, *Il6st*, *Il6* and *Il6ra* mRNA in MR13 vs 4T1 tumor cells.

(d) Fraction of Sca-1⁺ population in MR13 tumor cells treated for 48 hours with Ruxolitinib (5 μ M) relative to vehicle control (DMSO) treatment.

(e) Illustrative scheme of the experimental design for testing the effect of Ruxolitinib on MR13 metastatic capacity shown in **f**. MR13 tumor cells were treated with Ruxolitinib or DMSO *in vitro* for 72 hours and then injected into the mice tail vein. Lungs were examined for metastasis 10 days after tumor cell injection.

(f) Number of metastatic nodules in the lungs from mice injected with MR13 treated *in vitro* with Ruxolitinib or DMSO and indicated (n=8).

Data are represented as mean values \pm SEM. P values: ns, non-significant, *** < 0.001, (unpaired two-tailed student's t test, and with Bonferroni correction for d)

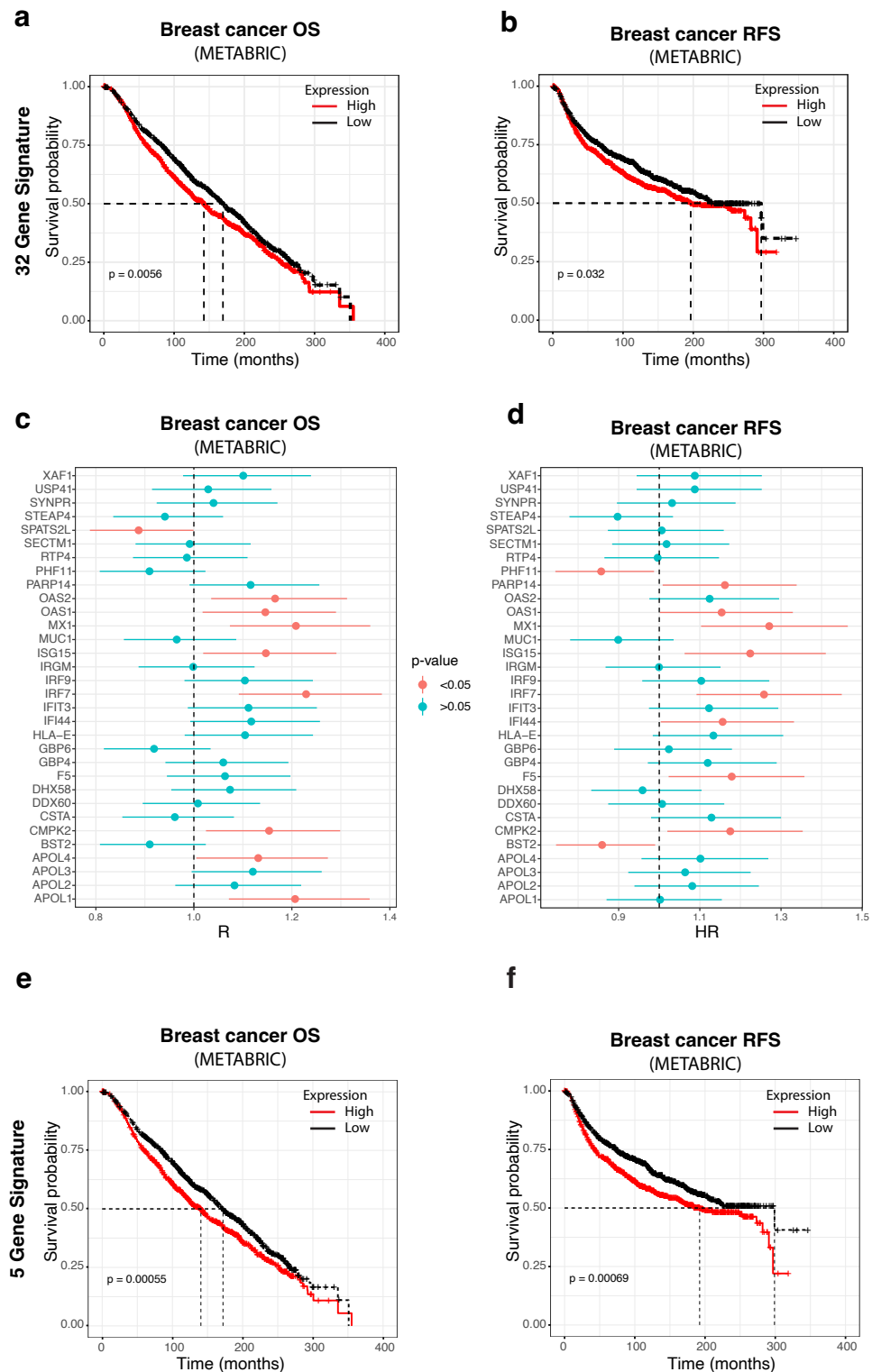


Figure 8

Figure 8. Tu-Gr1⁺CD11b⁺-induced tumor cell signature predicts worse outcome in breast cancer patients

(a-b) Kaplan-Meier curves showing overall survival (OS) **(a)** or relapse-free survival (RFS) **(b)** for breast cancer patients according to high or low expression of an orthologue 32 gene signature, based on the Tu-Gr1⁺CD11b⁺ -induced 4T1 cell signature, in the METABRIC datasets. The p-value was calculated using the log-rank test and high and low expression levels were stratified by median values.

(c-d) Forest plots showing the Cox proportional hazard regression (HR) for OS **(c)** and RFS **(d)** of the individual 32 orthologues of the Tu-Gr1⁺CD11b⁺-induced signature, based on gene expression in tumor samples from METABRIC dataset.

(e-f) Kaplan-Meier curves showing OS **(e)** and RFS **(f)** according to the reduced 5 orthologue gene signature. expression in the METABRIC datasets.

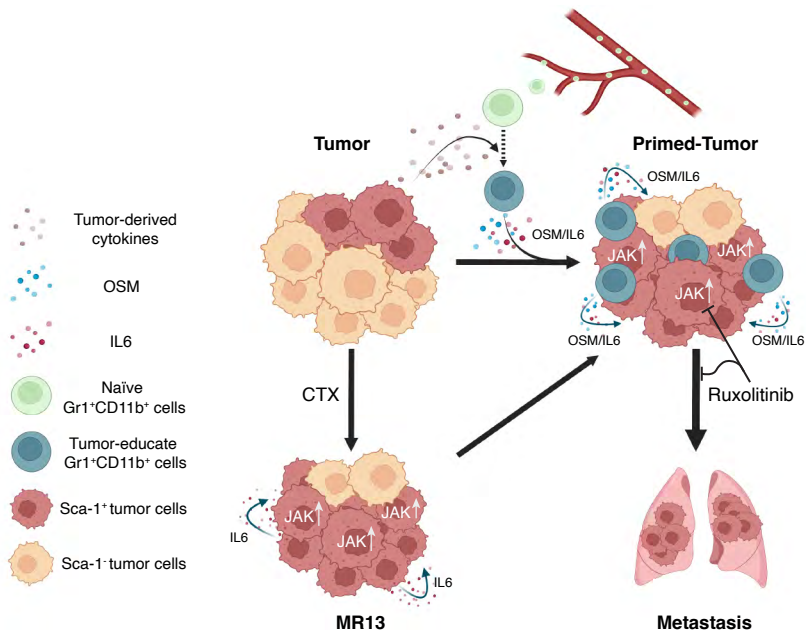
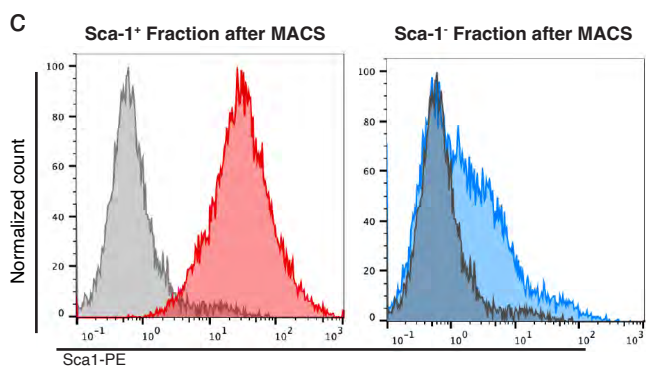
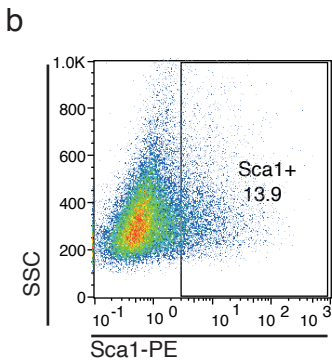
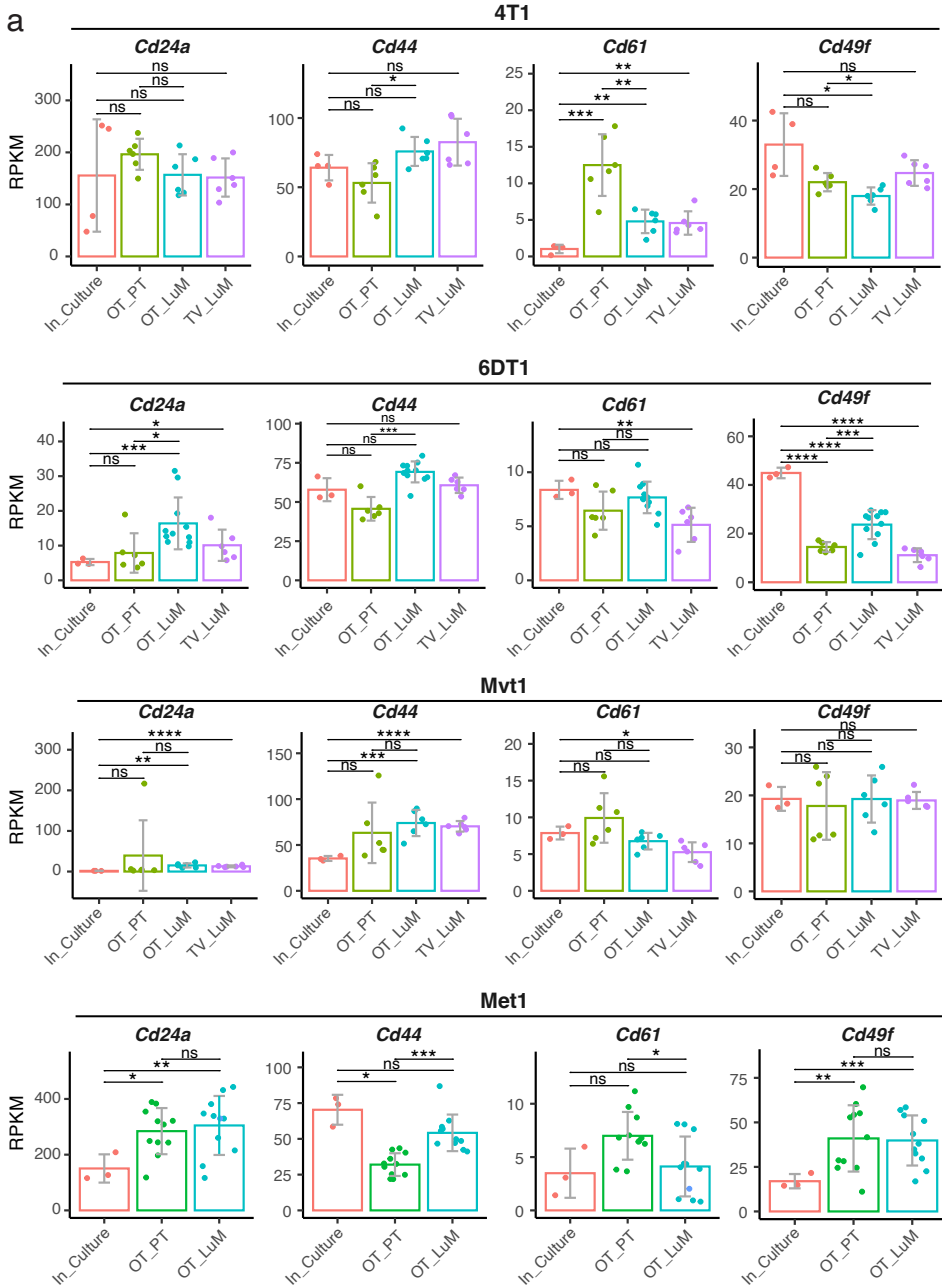


Figure 9

Figure 9 Illustrative scheme of the proposed model for cancer cell plasticity modulated by OSM/IL6 during tumor progression and chemotherapy

Parental tumor cells maintain a small portion of highly metastatic Sca-1⁺ population. During tumor progression, naïve Gr1⁺CD11b⁺ are recruited to the TME and educated into Tu-Gr1⁺CD11b⁺ by tumor-derived factors. In turn, Tu-Gr1⁺CD11b⁺ secrete OSM and IL6 to convert Sca-1⁻ population into a highly metastatic Sca-1⁺ population. Chemotherapy (CTX) enriched for Sca-1⁺ population due to its intrinsic resistance against cytotoxic treatment. Resistant cells express IL6 to maintain the high portion of Sca-1⁺ population with high metastatic ability. JAK inhibitor Ruxolitinib suppresses the conversion to Sca-1⁺ population and metastasis. Inhibition of OSM, IL6 and the activated downstream kinase JAK are candidate therapeutic targets to impinge on metastatic breast cancer progression during natural evolution and following therapy-resistance.

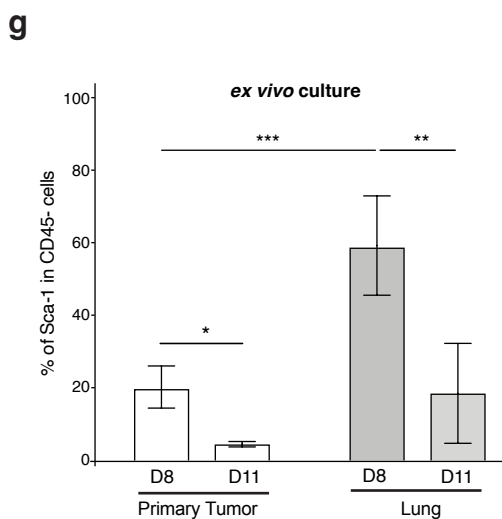
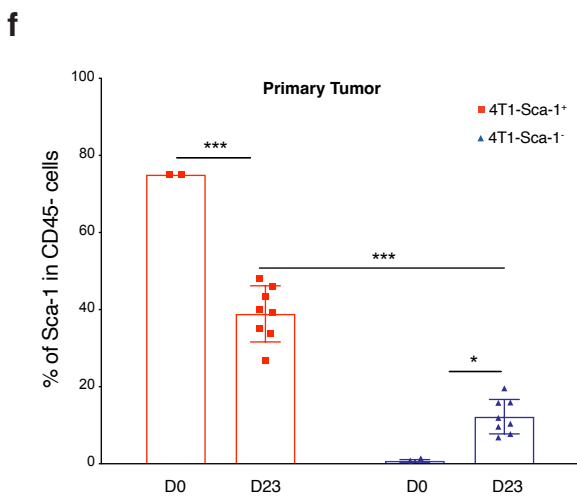
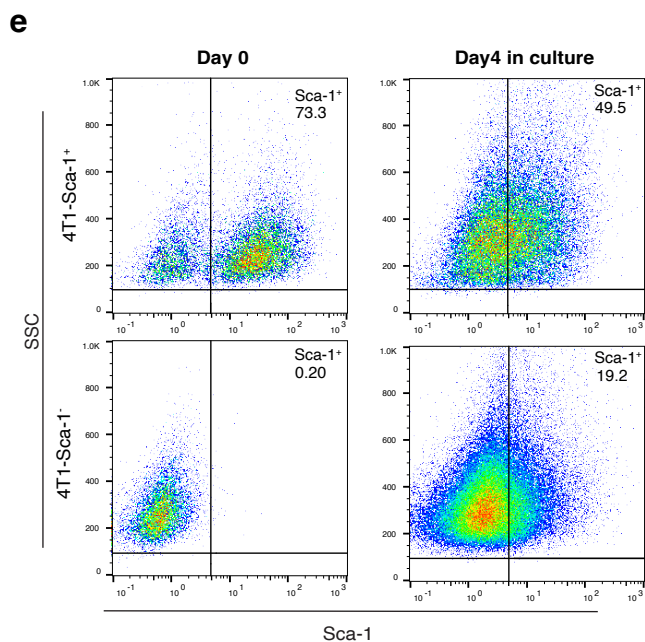
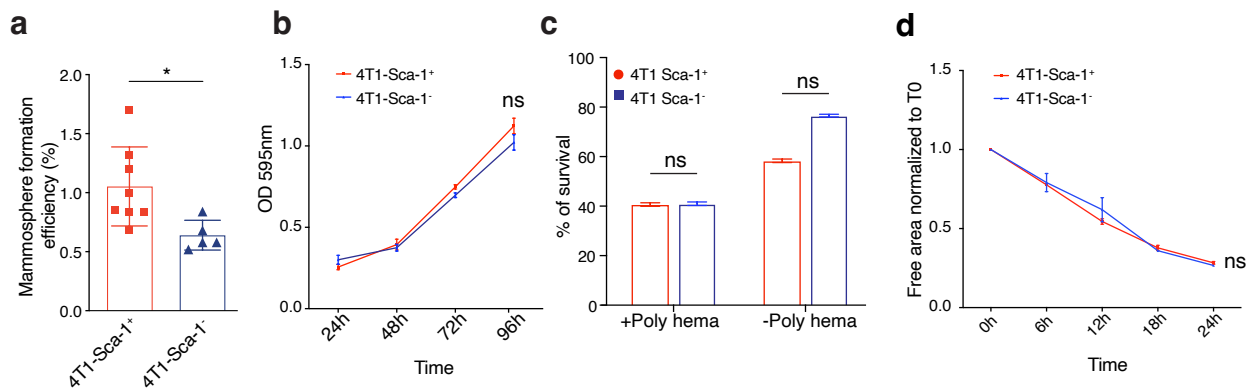


Supplementary Fig 1. Stem cell markers expression in multiple metastatic breast cancer models

(a) Stem cell marker *Cd24a*, *Cd44*, *Cd61* and *Cd49e* mRNA expression in 4T1, 6DT1, Mvt1 and Met1 metastatic murine breast cancer models extracted from Ross dataset. Data are presented as mean values of RPKM \pm SD. *, $p < 0.05$; **, $p < 0.01$; ***, $p < 0.001$; ****, $p < 0.0001$; ns, non-significant (unpaired two-tailed student's t test).

(b) Dot plot representation of Sca-1 expression in 4T1 parental cell line determined by flow cytometry.

(c) Histogram of Sca-1 expression distribution on MACS positively selected Sca-1⁺ cells (red histogram) and MACS negatively selected Sca-1⁻ cell (blue histogram). Gray: histogram of fluorescence of unstained cells.



Supplementary Fig 2. Sca-1⁺ tumor cells have stem cell-like features *in vitro* and show plasticity *in vivo* and *in vitro*

(a) Quantification of the mammosphere forming efficiency of 4T1-Sca-1⁺ and 4T1-Sca-1⁻ populations.

(b) Cell proliferation curve of 4T1-Sca-1⁺ and 4T1-Sca-1⁻ *in vitro* MACS isolated tumor cells determined by crystal violet assay. The results represent optical density (OD) of the wells.

(c) Anchorage-independent survival of 4T1-Sca-1⁺ and 4T1-Sca-1⁻ MACS isolated tumor cells determined with an anoikis assay. Cells were cultured in control or poly-hema coated wells (to avoid adhesion) and viability measured by annexin/PI staining and FACS analysis. The results are shown as % of viable cells identified as Annexin V negative and PI negative cells.

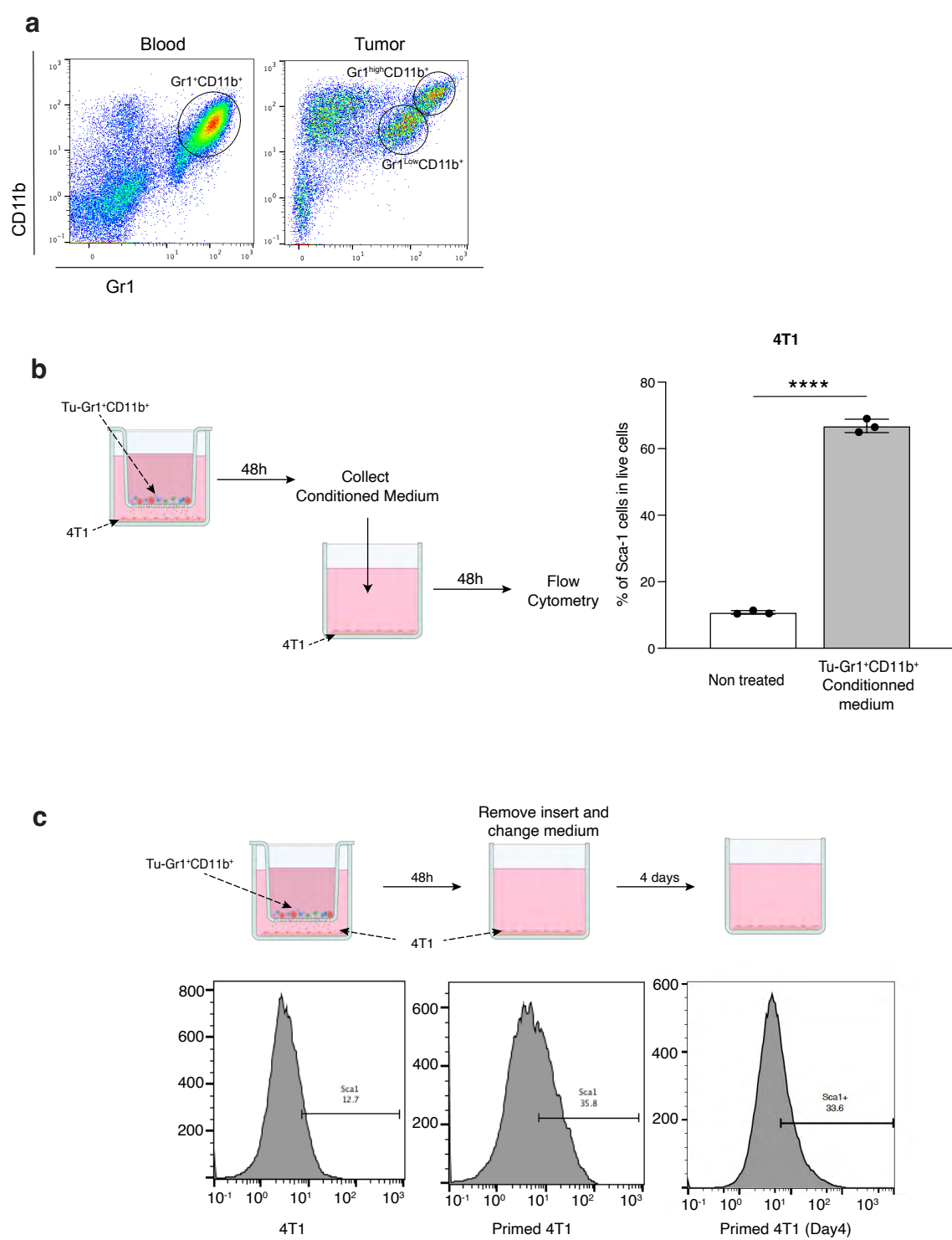
(d) Cell motility of 4T1-Sca-1⁺ and 4T1-Sca-1⁻ sorted tumor cells determined by a scratch wound healing assay (n=5-6/group). Results are given cell-free area relative to the initial wound area.

(e) The abundance of Sca-1⁺ population after MACS isolation from parental 4T1 cells. Day 0: immediately after positive sorting, the Sca-1⁺ population to accounts for 73.3% of total cells (upper panel). After 4 days of *in vitro* culture the abundance of the Sca-1⁺ population decreased to 48.9%. Negatively sorted Sca-1⁻ population accounts for >99 % of total cells (lower panel). After 4 days of *in vitro* culture 19.2% of the initially Sca-1⁺ cells were Sca-1⁺.

(f) Abundance of Sca-1⁺ population at the time of orthotopic injection of MACS isolated 4T1-Sca-1⁺ and 4T1-Sca-1⁻ cells into the mammary fat pad of BALB/C mice (D0) and in the derived primary tumors 23 days post injection (D23) as indicated. n=3-8/group.

(g) Abundance of the Sca-1⁺ population in tumor cells recovered from primary tumors and lung metastases 21 days post orthotopic injection and further cultured for 8- and 11-days *ex vivo* as indicated.

Data represent mean values \pm SEM from 3 independent experiments. *, $p < 0.05$; **, $p < 0.01$; ***, $p < 0.001$; (unpaired two-tailed student's t test).

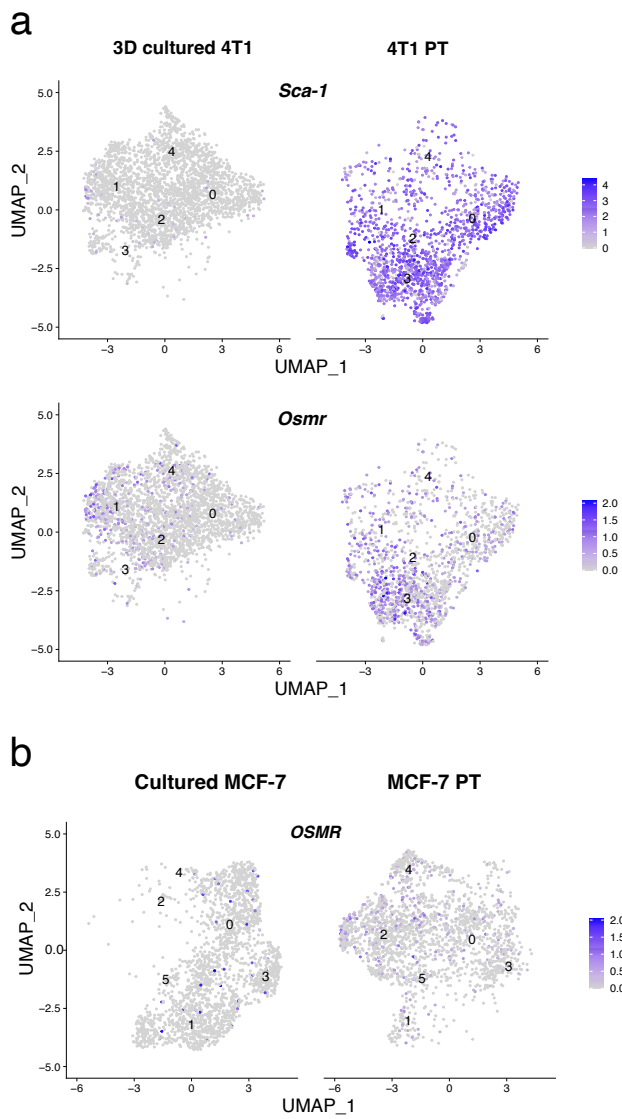


Supplementary Fig 3. Tu-Gr1⁺CD11b⁺-derived secreted factors promote the enrichment of Sca-1⁺ population

(a) Dot plots presenting Gr1⁺CD11b⁺ subpopulations in Blood and Tumor site of 4T1 tumor-bearing mice.

(b) Abundance of the Sca-1⁺ population in tumor cells cultured for 48 hours in the presence of medium collected from 4T1/Tu-Gr1⁺CD11b⁺ cocultures (48 hours). Sca-1 expression on 4T1 cells was determined by flow cytometry.

(c) Sca-1 expression in parental 4T1 cells (left panel), 4T1 primed for 2 days with Gr1⁺CD11b⁺ cells (middle panel) and cultured for 4 additional days in the absence of Gr1⁺CD11b⁺ (right panel). Sca-1 expression was determined by flow cytometry.

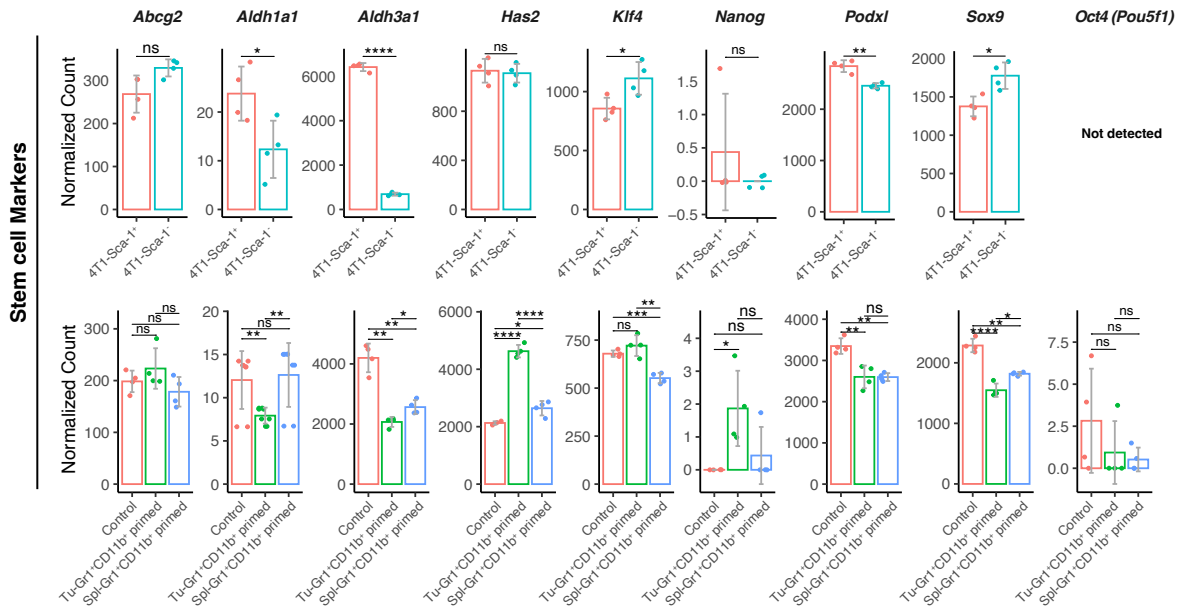
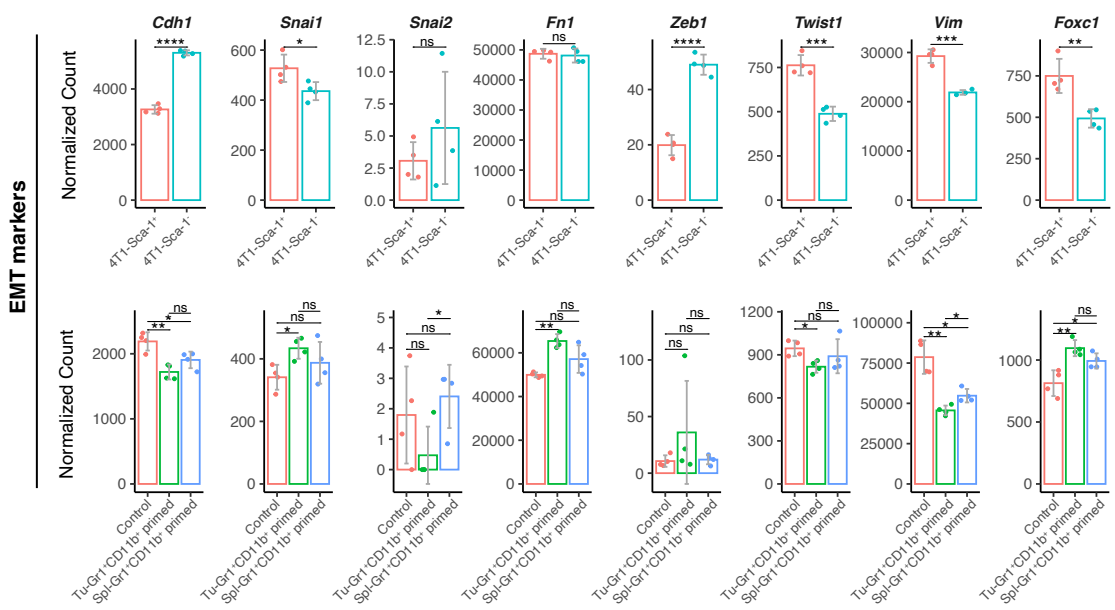


Supplementary Fig. 4

Supplementary Fig 4. TME expands the Sca1⁺ population during *in vivo* tumor progression

(a) UMAP plots showing the expression of *Sca-1* and *Osmr* in 4T1 tumor cells in 3D culture or primary tumors (PT). Analysis based on publicly available data (GSM4812003 and GSM3502134)

(b) UMAP plot showing the expression of *OSMR* in MCF-7 tumor cells in culture or primary tumors (PT). Analysis based on publicly available data (GSM4681765 and GSM5904917).

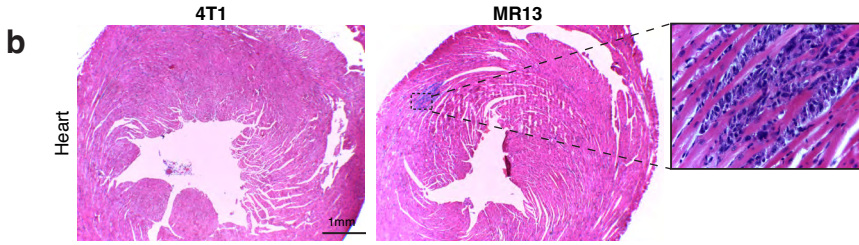
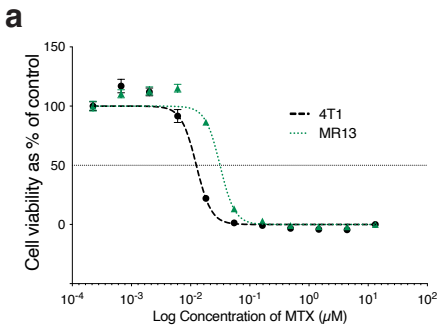
a**b**

Supplementary Fig. 5

Supplementary Fig 5. Expression of selected stem cell/CSC and EMT genes in 4T1-Sca-1⁺, 4T1-Sca-1⁻ and differently primed 4T1 cells

Expression of stem cell markers **(a)** and EMT markers **(b)** in 4T1-Sca-1⁺ cells, 4T1-Sca-1⁻ cells, and parental, Tu-Gr1⁺CD11b⁺-educated, Spl-Gr1⁺CD11b⁺-educated 4T1 cells, as indicated.

Data represent mean values of RPKM \pm SD. *, $p < 0.05$; **, $p < 0.01$; ***, $p < 0.001$; ****, $p < 0.0001$ (unpaired two-tailed student's t test, and with Bonferroni correction for MDSC-educated 4T1 cells).

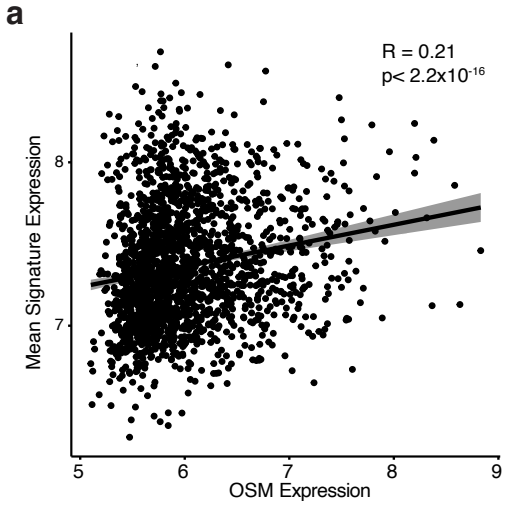


Supplementary Fig. 6

Supplementary Fig 6. Sca-1⁺ enriched 4T1 cells and MR13 cells are more resistant to chemotherapy drugs

(a) Dose dependent effect of 48 hours treatment with MTX on 4T1 and MR13 cells' viability. IC₅₀ of MTX for 4T1 and MR13 are 12.5 nM and 31.4 nM respectively.

(b) Illustrative H&E stained heart sections of BALB/c mice 22 days post orthotopic injection with 4T1 cells (left) or MR13 cells (right and insert) (n=8-9/group).



Supplementary Fig. 7

Supplementary Fig 7. Genes of the Tu-Gr1⁺CD11b⁺-induced signature and patients' outcome

(a) Correlation of the orthologue 32 gene signature, based on the Tu-Gr1⁺CD11b⁺ - induced signature, with *OSM* expression in the METABRIC datasets. Spearman's correlation coefficients and p-values are shown.